國立交通大學

半導體材料與製程產業碩士專班

碩士論文

GaAsSb 緩衝層對於 InAs/GaAs 系統中量子點結構與性質之效應

The effect of GaAsSb buffer layer on InAs quantum dots in GaAs

研究生：林珮吟

指導教授：張立 博士

中華民國九十六年七月

GaAsSb 緩衝層對於 InAs/GaAs 系統中量子點結構與性質之效應

The effect of GaAsSb buffer layer on InAs quantum dots in GaAs

研究生：林珮吟　　Student：Pei-Yin Lin

指導教授：張 立 博士　　Advisor：Dr. Li Chang

國立交通大學

半導體材料與製程產業碩士專班

碩士論文

A Thesis
Submitted to Industrial Technology Research and Development Master Program
on Semiconductor Materials and Processing
College of Engineering
National Chiao Tung University
in Partial Fulfillment of the Requirements
for the Degree of Master of Science
in

Semiconductor Materials and Processing

July 2007

Hsinchu, Taiwan, Republic of China

中華民國九十六年七月

GaAsSb 緩衝層對於 InAs/GaAs 系統中量子點結構與性質之效應

研究生：林珮吟　　　　指導教授：張立 博士

國立交通大學半導體材料與製程碩士專班

摘要

本研究目的在於了解 InAs/GaAs 系統中 GaAsSb 緩衝層對 InAs 量子點的光學及結構性質之影響。以分子束磊晶法(MBE)先成長 1nm 厚的三組不同 Sb 濃度的 $GaAs_{1-X}Sb_X$ 緩衝層於 GaAs 基材上，其緩衝層的組成分別為(X=0%、5.72%、11.44%)，接著成長 InAs 量子點，最後再成長 GaAs 覆蓋層於 InAs/GaAsSb 結構上。利用二次離子質譜儀(SIMS)及附加於 TEM 的 X 光能量散佈光譜儀(EDS)分析 Sb 於量子點結構中的分佈情形；使用光激發光譜(PL)及穿透式電子顯微鏡(TEM)來觀察以先成長 GaAsSb 緩衝層對 InAs 量子點光學性質及結構性質的影響。由 PL 光譜的發光性質可得知量子點的尺寸及分布情形；TEM 分析可得知量子點的尺寸及密度。PL 的結果發現，成長以 GaAsSb 做為 InAs 量子點結構中的緩衝層，造成的發光波長紅移；並由 TEM 影像觀察得知確實增加了量子點的尺寸，但對於量子點的密度無明顯的改變。此外，本論文亦就光學及結構性質與量子點的尺寸和分布之關係加以討論。

The effect of GaAsSb buffer layer on InAs quantum dots in GaAs

Student：Pei-Yin Lin Advisor：Dr. Li Chang

Industrial Technology Research and Development Master Program on
Semiconductor Materials and Processing
National Chiao Tung University

ABSTRACT

This work studies the effect of GaAsSb buffer layer of different Sb concentrations on the optical and structural properties of InAs quantum dots (QDs) embedded in GaAs. The InAs/GaAs QD structures were grown by molecular beam epitaxy (MBE), which contained the buffers of $GaAs_{1-X}Sb_X$ (X = 0%, 5.72%, and 11.44%) of 1 nm thickness on the GaAs substrates, and finally capped with a 300-nm-thick GaAs layer. In this thesis, the secondary ion mass spectrometry (SIMS) and energy dispersive X-ray spectroscopy (EDS) were used to investigate the distribution of Sb in the QD structures. Photoluminescence (PL) measurements and transmission electron microscopy (TEM) were performed to investigate the optical and structural properties of QDs. The embedded InAs dots were observed by high-angle annular dark field-scanning TEM (HAADF-STEM). PL spectra show the size and distribution of QDs, and TEM images show that the dots size and density. PL spectra reveal that the GaAsSb buffer layer in InAs QD structures has a wavelength redshift. TEM images exhibit the dots size increases with the concentration of Sb in the buffer layer, but with an insignificant increase in density. There is a further discussion about the relation between the optical and structural properties of QDs and the size and distribution.

Acknowledgements

此時此刻的心情是溢於紙筆所能表達的…。

回首兩年，最感謝的人莫過於我的指導教授—張立教授。感謝老師，在我初進研究所面談之時，就願意給予我如此好的學習機會；感謝老師，在老師用心又細心的指導下，每週的個別報告讓我磨練許多，而老師平日對於學生的關心和對論文的反覆修改和叮嚀更是令人感動；感謝老師，在老師自由的風氣下，讓我知道自我約束及要求；感謝老師，老師對於研究的執著和認真，以及從不疾言厲色且溫文儒雅的個性下薰陶，讓我見識到學者的風範而總是對老師心服誠悅。在老師的指導下，我很高興的對自己說：我從沒有後悔選擇就讀交大。而老師擁有超帥的外表兼具讀書人的內在，並且氣質中散發出害羞又帶著靦腆笑容的獅子座個性的淳樸台南人，真是讓全師奶界以及少女界為之風靡！

感謝清大工科系—陳福榮教授、交大電物系—陳振芳教授以及交大材料系—謝宗雍教授，三位老師對於學生論文的指導，使得本論文更加完整而嚴謹。

超級感謝實驗室的岳翰學長，謝謝學長這兩年的指導以及高超又強大的 TEM 分析技術支援，沒有學長就不會有這本論文的誕生。感謝厚光學長、志坤學長、智偉學長、家豪學長、東杰學長、尉霖學長、學業愛情兩得意的峻彥同學兼學長、一起跳皮拉提斯的欣怡同學、一起熬夜趕論文加昏睡在實驗室的炯朝同學、議森學弟、坤安學弟、勝民學弟、原安學弟、志盛學弟等人的陪伴，能夠跟大家在同一個實驗室真棒！感謝認識十三年且同為新竹淪落人的姐妹淘：奎君跟怡婷，謝謝妳們真的是從小到大的陪伴！感謝在研究所認識的好友：林宏洲實驗室的光潔、宗琦、玄之、岳勳、柏儒，林健正實驗室的鎮基，為兩年的研究生活增添更多歡笑！感謝大學時代的專題實驗室，國立中興大學化工系邱信程教授以及曾經一起打拼過的夥伴們，還有提前離開到另一個世界去打太鼓達人的健銘；感謝因為有你們的支持，才成就今日的我。

最後感謝我的家人—奶奶、爸爸、媽媽、姊姊、哥哥、嫂嫂、即將報到的小姪子、以及大阿姨一家人，還有在天上摯愛的外婆。雖然一路走來並非平順、而前方的路充滿未知，但你們是我持續前進的動力～

珮吟　2007.08.31　於新竹交大

Contents

Abstract (in Chinese) i

Abstract (in English) ii

Acknowledgements iii

Contents iv

Figure Captions vi

Table Captions ix

Chapter 1 Introduction 1

1.1. Introduction to Quantum Dots 1

1.1.1. The Formation of Self-assembled Quantum Dots 2

1.1.2. The Characteristics and Applications of Quantum Dots 5

1.2. Literature Review 6

1.3. Motivation 14

Chapter 2 Sample Fabrication and Experimental Design 15

2.1. Molecular Beam Epitaxy Growth of InAs Quantum Dots 15

2.2. Analytical Techniques 18

2.2.1. Secondary Ion Beam Spectroscopy 18

2.2.2. Photoluminescence 20

2.2.3. Transmission Electron Microscopy 21

2.3. Preparation of TEM Specimens 25

2.3.1. Plan-view TEM Specimens 26

2.3.2. Cross-sectional TEM Specimens 27

Chapter 3 Results and Discussion 28

3.1. SIMS 28

3.2. PL 31

3.2.1. Power-Dependence 31

3.2.2. Temperature-Dependence 36

3.3. Cross-sectional TEM 39

3.4. Plan-view TEM 45

3.5. The Analysis of Chemical Distribution 48

3.6. Discussion 52

Chapter 4 Summary 55

References 57

Appendixes 62

A. Monte Carlo Simulation 62

B. Desktop Spectrum Analyzer Simulation 63

Figure Captions

Figure 1.1 Semiconductor structures and corresponding electronic density of states near the edge of electronic bands. (a) Bulk, (b) quantum well, (c) quantum wire, and (d) quantum dot. 2

Figure 1.2 Schematic diagrams of three growth modes for heteroepitaxial systems and evolution of growth. (a) FM mode, (b) VW mode, and (c) SK mode. 4

Figure 1.3 Schematic diagrams of strains in the three growth modes for heteroepitaxial systems that can be distinguished. (a) FM mode, (b) VW mode, and (c) SK mode. 4

Figure 1.4 Room temperature bandgap energy versus lattice constant of common elemental and binary compound semiconductors. 5

Figure 1.5 Base diameter and density of the uncapped islands measured by AFM as a function of growth rate. 10

Figure 1.6 The optical properties of QDs are significantly affected by different substrate temperature. (a) 4.2 K and (b) room temperature. 11

Figure 1.7 AFM images of corresponding uncapped QDs grown at (a) 480 °C and (b) 530 °C. The dots density approximately of 1×10^{11} cm^{-2} and 1.2×10^{10} cm^{-2}, respectively. 11

Figure 1.8 (110) cross-sectional TEM and HAADF-STEM images of (a) uncapped InAs dots and (b) InAs dots covered by GaAs layer. 12

Figure 1.9 Schematic band diagrams of (a) InAs/InGaAs/GaAs and (b) InAs/GaAsSb/GaAs structures. 12

Figure 1.10 The room temperature photoluminescence spectra of GaAs and $GaAs_{0.83}Sb_{0.17}$ capped InGaAs QDs. 13

Figure 1.11 The room temperature photoluminescence spectra of GaAs and $GaAs_{0.98}Sb_{0.02}$ buffer both with the dot density of 3×10^{10} cm^{-2}. 13

Figure 2.1 Schematic views of three samples for the structures and growth conditions. 16

Figure 2.2 Schematic diagrams of three samples for their energy gap. 17

Figure 2.3 Equilibrium phase diagram in the function of the coverage H in monolayer and lattice misfit ε. 18

Figure 2.4 The schematic diagram (left panel) and the TEM image (right panel) of DP for InAs/GaAs QD structures. 25

Figure 2.5 Schematic diagrams of (a) plan-view specimen on the supporter and (b) cross-sectional specimen. 27

Figure 3.1 SIMS depth profile of sample 1 (0% Sb) in the QD structures. 29

Figure 3.2 SIMS depth profile of sample 2 (5.72% Sb) in the QD structures. 30

Figure 3.3 SIMS depth profile of sample 3 (11.44% Sb) in the QD structures. 30

Figure 3.4 Excitation power dependent PL spectra from sample 1 at room temperature........ 32

Figure 3.5 Excitation power dependent PL spectra from sample 2 at room temperature........ 32

Figure 3.6 Excitation power dependent PL spectra from sample 3 at room temperature........ 33

Figure 3.7 PL spectra from InAs/$GaAs_{1-X}Sb_X$ (X = 0, 0.0572, and 0.1144) QD structures with 1.3 mW excitation power at room temperature. 33

Figure 3.8 PL spectra from InAs/$GaAs_{1-X}Sb_X$ (X = 0, 0.0572, and 0.1144) QD structures with 65 mW excitation power at room temperature. 34

Figure 3.9 The wavelength of PL peaks in the GS and ES with 1.3 and 65 mW excitation powers at room temperature as a function of Sb concentration in the buffer layer. 34

Figure 3.10 The FWHM of PL peaks in the GS and ES with 1.3 and 65 mW excitation powers at room temperature as a function of Sb concentration in the buffer layer. 35

Figure 3.11 PL spectra of sample 1 with 0.13 mW excitation power at variable temperatures. 37

Figure 3.12 PL spectra of sample 2 with 0.13 mW excitation power at variable temperatures. 37

Figure 3.13 PL spectra of sample 3 with 0.13 mW excitation power at variable temperatures. 38

Figure 3.14 The emission wavelength of PL peaks in the GS and ES with 0.13 mW excitation power as a function of temperature. 38

Figure 3.15 The FWHM of PL peaks in the GS and ES with 0.13 mW excitation power as a function of temperature. 39

Figure 3.16 [100] Cross-sectional BF TEM image of sample 1 (0% Sb)............................... 40

Figure 3.17 [100] Cross-sectional BF TEM image of sample 2 (5.72% Sb).......................... 41

Figure 3.18 [100] Cross-sectional BF TEM image of sample 3 (11.44% Sb)........................ 41

Figure 3.19 [100] Cross-sectional DF (400) TEM image of sample 1 (0% Sb)...................... 42

Figure 3.20 [100] Cross-sectional DF (400) TEM image of sample 2 (5.72% Sb)................. 42

Figure 3.21 [100] Cross-sectional DF (400) TEM image of sample 3 (11.44% Sb).............. 43

Figure 3.22 The distribution of cross-sectional TEM strain field width of QDs.................... 43

Figure 3.23 The distribution of cross-sectional TEM strain field height of QDs................... 44

Figure 3.24 Plan-view BF TEM image of sample 1 (0% Sb) under two-beam conditions..... 45

Figure 3.25 Plan-view BF TEM image of sample 2 (5.72% Sb) under two-beam conditions.46

Figure 3.26 Plan-view BF TEM image of sample 3 (11.44% Sb) under two-beam conditions. 46

Figure 3.27 The distribution of plan-view TEM [100] strain field.. 47

Figure 3.28 The distribution of plan-view TEM [010] strain field.. 47

Figure 3.29 [100] Cross-sectional HAADF-STEM image of sample 3 (11.44% Sb). 49

Figure 3.30 The chemical distribution around the QD and the wetting layer of sample 3...... 49

Figure 3.31 The atomic percentages and EDS spectra of different regions of sample 3......... 50

Figure 3.32 The EDS spectra of the experimental result of chemical composition in the dot center and the DTSA simulation of $In_{0.50}As_{0.35}Sb_{0.15}$. 51

Figure 3.33 Schematic diagrams of (a) the formation of InAs QDs of samples 1 (0% Sb), 2 (5.72% Sb) and 3 (11.44% Sb), (b) the diffusion of Sb, (c) capping of GaAs layer. 54

Table Captions

Table 2.1 For bulk materials, GaAsSb lattice constant and InAs/GaAsSb lattice mismatch of samples 1, 2 and 3, respectively. 17

Table 3.1 The wavelength and FWHM in the ground state and excited state with 1.3 and 65 mW excitation powers at room temperature of three samples. 35

Table 3.2 Cross-sectional TEM of the strain filed width and height of QDs..........................44

Table 3.3 Plan-view TEM of [100] and [010] strain filed and average density of QDs. 48

Chapter 1 Introduction

1.1. Introduction to Quantum Dots

In 1969, Esaki and Tsu proposed to use a semiconductor superlattice based on a periodic structure of alternating layers of semiconductor materials with wide and narrow band gaps [1]. From then on, the research in quantum nanostructures is thriving.

The wave function of electrons is going to change when they are confined to dimensions comparable with their wavelength. Low threshold considerations dictate the transition from bulk to quantum well to quantum wire to quantum dot systems [2]. Figure 1.1 shows that confining electrons to small structures causes the continuous bulk bands to split up into discrete levels [3]. A quantum well is a potential well that confines electrons, which were originally free to move in three dimensions, to two dimensions, forcing them to occupy a planar region. The effects of quantum confinement take place when the quantum well thickness becomes comparable at the de Broglie wavelength of the carriers, leading to energy levels called energy subbands. For the quantum wire, the electrons in two dimensions are quantized and in one dimension electrons are free to move. And finally, confining electrons to three dimensions forms a quantum dot (QD).

Being quasi-zero-dimensional nanostructures, QDs have a discrete density of states and wave function properties. The confinement can be due to electrostatic potentials, the presence of an interface between different semiconductor materials, the presence of the semiconductor surface, or a combination of above. In contrast to atoms, the energy spectrum of a QD can be engineered by controlling the geometrical size, shape, and the strength of the confinement potential. Such dots are sometimes called "artificial atoms". In a crystal, the periodic atomic potential leads to band formation. But in a superlattice, an artificial, human-made periodical potential causes the formation of small bands. Thus, the utilization of QDs is one of the most promising technologies for applications in optoelectronic devices and lasers.

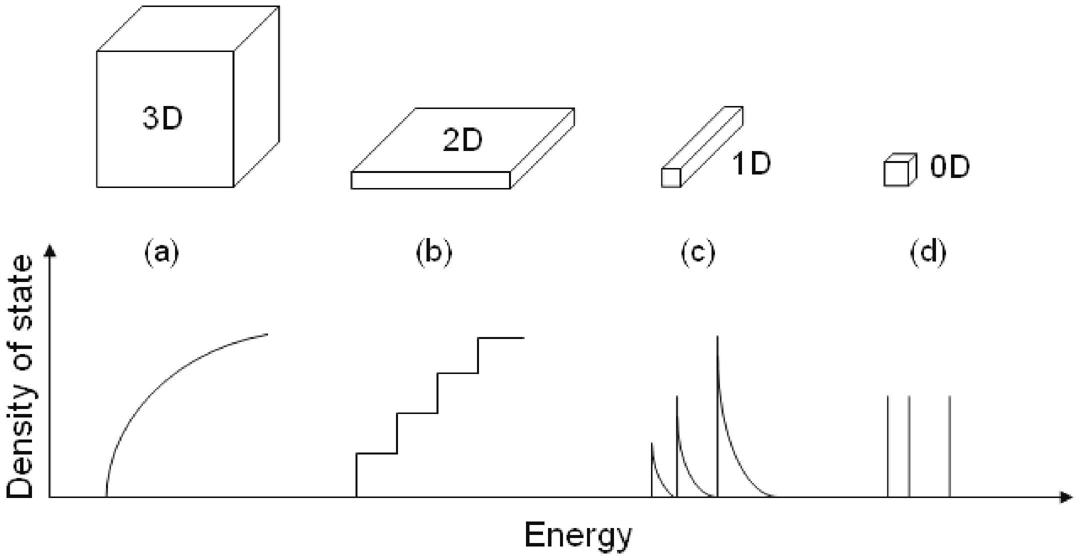

Figure 1.1 Semiconductor structures and corresponding electronic density of states near the edge of electronic bands. (a) Bulk, (b) quantum well, (c) quantum wire, and (d) quantum dot [3].

1.1.1. The Formation of Self-assembled Quantum Dots

In the equilibrium theory of heteroepitaxial growth, three growth modes are traditionally distinguished [4]:

(1) Frank-van der Merwe (FM mode):

If the sum of the epilayer surface energy and the interface energy is lower than the energy of the substrate surface, the FM mode occurs. It may be described as two-dimensional layer-by-layer growth.

(2) Volmer-Weber (VW mode):

If the sum of the epilayer surface energy and the interface energy is higher than the energy of the substrate surface, the VW mode occurs. It may be described as three-dimensional island growth.

(3) Stranski-Krastanow (SK mode):

For a strained epilayer with small interface energy, the deposited layer initially grows as a two-dimensional wetting layer. As the thickness of wetting layer increases, the strain energy in the deposited layer increases. This layer can lower its energy by forming three-dimensional isolated islands in order to release the strain. The SK growth mode leads to a two-dimensional wetting layer with three-dimensional islands on top.

These growth modes are deduced from equilibrium considerations of the energy balance between the surface energy and the interface energy for lattice-matched systems. However, for heteroepitaxial growth of highly strained structures, the elastic strain energy associated with epitaxial lattice mismatch must be considered.

The SK growth mode is favorable for a layer with a lattice constant that differs considerably from that of the substrate, because the islands allow a relaxation of the strain energy. It also prefers to less differences between the epilayer surface energy and the substrate surface energy [5]. The SK growth mode may occur in systems where the formation of a two-dimensional wetting layer is favorable during the deposition of the first few monolayers (ML) of the film [6]. With the increasing layer thickness, the strain energy of two-dimensional wetting layer increases. Above the critical thickness, the onset of three-dimensional island formation on the substrate occurs, mainly because an island offers the possibility of relaxation of elastic strain at its free surface [7]. As a result of formation of such structures in nanometer size, what is called QDs, carriers in inlands are confined in three dimensions, as shown in Figures 1.2 and 1.3.

There has been considerable interest in using SK growth to deposit coherent islands, known as self-assembled QDs. Take InAs/GaAs QDs as an example. The lattice constant of InAs (a_{InAs} = 6.06 Å) is larger than GaAs (a_{GaAs} = 5.65 Å) and so has a compressive strain in the lateral direction after island formation. If the size of island exceeds a critical thickness that mainly depends on the misfit between the wetting layer and substrate, it is required for the generation of the misfit dislocations. However, if coherency is maintained within the critical condition, defect free and highly uniform QDs can result from the SK mode.

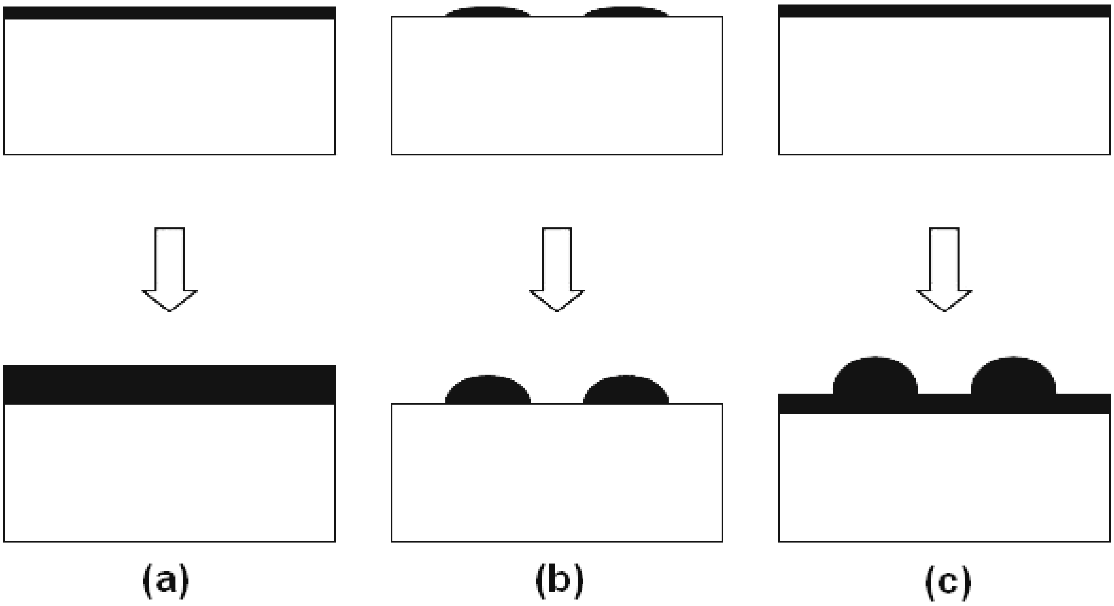

Figure 1.2 Schematic diagrams of three growth modes for heteroepitaxial systems and evolution of growth. (a) FM mode, (b) VW mode, and (c) SK mode [3].

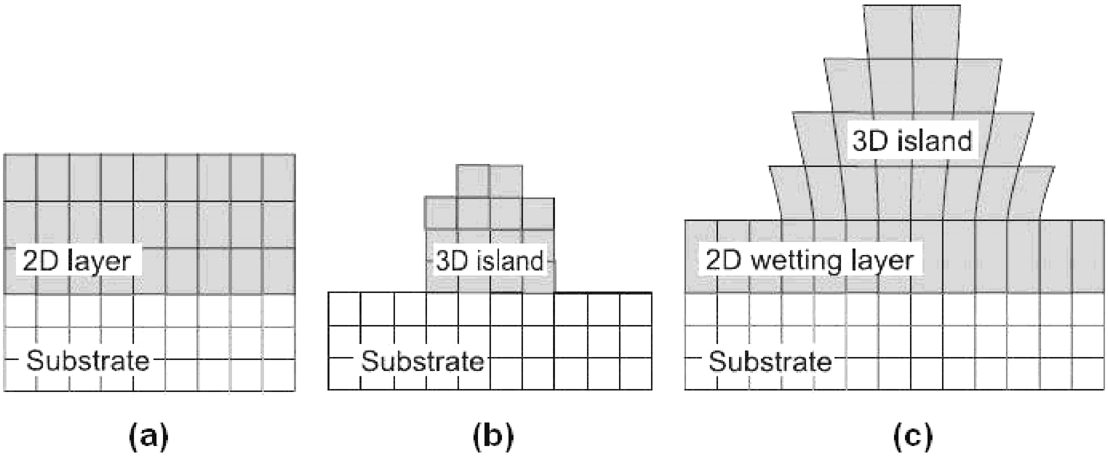

Figure 1.3 Schematic diagrams of strains in the three growth modes for heteroepitaxial systems that can be distinguished. (a) FM mode, (b) VW mode, and (c) SK mode [7].

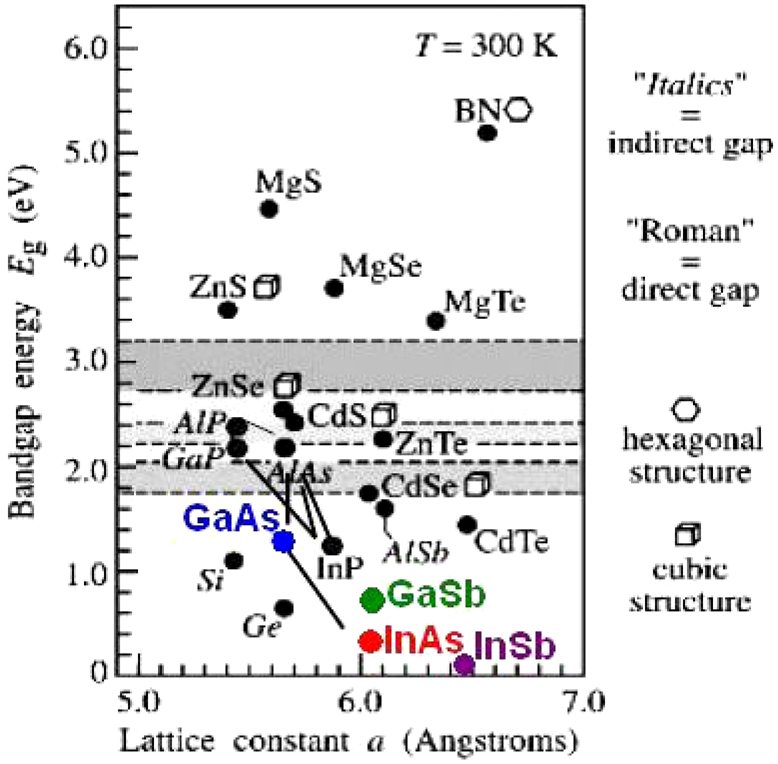

Figure 1.4 Room temperature bandgap energy versus lattice constant of common elemental and binary compound semiconductors [8].

1.1.2. The Characteristics and Applications of Quantum Dots

QD is a nanostructure that confines the motion of conduction band electrons, valence band holes, or excitons in all three spatial directions. Hence, a QD has a discrete quantized energy spectrum. The corresponding wave functions are spatially localized within the QD, but extend over many periods of the crystal lattice.

Using the structure of QD as an active region in a semiconductor laser is expected to exhibit superior lasing properties such as higher efficiency of electron confinement, lower threshold current density, lower transparency current density, higher differential gain, higher characteristic temperature, higher temperature stability, and wide modulation bandwdith, and so forth. Therefore, semiconductor of QDs has important potential applications in optoelectronic devices.

QDs are particularly significant for optoelectronic applications due to their theoretically high quantum yield. As a result, they have superior transport and optical properties, and are being studied for use in single electron transistor, quantum dot lasers, amplifiers, and biological sensors. According to recently researches, the emission spectra for QD lasing in these applications are 1.3~1.6 μm.

1.2. Literature Review

With the development of telecommunication infrastructure, the need for high data transmission rates has increased. To reach higher data transmission rates, the frequency of the electromagnetic radiation must correspondingly increase. The modern fiber-optic communication must rely on high performance semiconductor lasers, so as to transmit high volume and low loss optical signals to further distance without repeaters. Moreover, high performance semiconductor lasers are essential for the establishment of high speed internet infrastructure. In order to reach high transmission rate and narrow beam divergence lasers are needed. However, InAs QDs grown by self-assembled techniques on GaAs substrates are affected by compressive strain from GaAs so that their emission wavelengths are usually around 1 μm. Several methods have been developed to reduce the effect of compressive strain and thus realize the longer wavelength emission. The related results about the modifications of heterojunction are summarized as following.

(1) The growth rate of InAs QDs

By growing InAs QDs at lower growth rate (<0.01 ML/s) can increase the dots size. Nakata *et al.* have found that the emission wavelength exceed 1.3 μm when the growth rate was reduced to 2×10^{-3} ML/s, but the island density decreased to 5×10^{9} cm^{-2} [9]. The InAs islands were grown on a GaAs/AlGaAs/GaAs buffer layer on Si-doped GaAs (001) substrates at 620 °C by molecular beam epitaxy and covered with a cladding layer.

Figure 1.5 illustrates that base diameter and density of the uncapped islands measured by AFM as a function of growth rate. A reduction in the growth rate enhances the migration length of In adatoms, allowing them to incorporate into already existing QDs instead of nucleating new structures. Therefore, the dots size can be significantly increased but the dots density decreases drastically, being in the low 10^9 cm^{-2} ranges.

(2) The substrate temperatures (Ts)

Chu *et al.* and Trofimov *et al.* have grown InAs QDs deposited onto GaAs by molecular beam epitaxy at different substrate temperatures [10, 11]. They both showed that the higher substrate temperature leads to the lower density of InAs QDs in large size on the surface.

Chu *et al.* grew four samples of 2.5 ML InA s QDs at different substrate temperatures Ts = 480, 500, 530 and 550 °C by molecular beam epitaxy [10]. The photoluminescence spectra were measured at 4.2 K and room temperature, as shown in Figure 1.6. At 4.2 K, the photoluminescence peak clearly shifts systematically to lower energies for temperature increase from 480 °C to 530 °C. The QDs become larger with the increasing substrate temperature. The diffusion length of the adatoms is mainly responsible for the changes in size of the QDs when substrate temperature is varied. Around a nucleation center which acts as sink for surrounding adatoms, there is an effective zone within which the adatoms are collected. This results in the formation of large islands at higher substrate temperatures. At 530 °C, two distinct photoluminescence peaks corresponding to the optical transition between the ground state and the first excited state of the QDs were observed. In reference to the QDs grown at 530 °C, the photoluminescence spectrum of the QDs grown at 550 °C shifts to higher energies, and three peaks can be clearly observed. Similar behavior is observed in the room temperature photoluminescence spectra.

The QDs density is also dependent on the substrate temperature because the dots density of the nucleation centers is sensitively dependent on the surface diffusion of the adatoms, as shown in Figure 1.7. Due to the smaller islands exclusion zone, there are more nucleation centers forming at low substrate temperatures, which give rise to a high density of QDs. Therefore, growing QDs on a higher substrate temperature leads to form larger dot size in a more homogeneous distribution which also results in the longer wavelength and the narrow distribution of the photoluminescence spectra.

(3) Uncapped and capped layer on InAs QDs

Quivy *et al.* and Ohtusbo *et al.* both have compared the uncapped and capped GaAs layer on InAs QDs by molecular beam epitaxy [12, 13]. The uncapped InAs QDs take the pyramidal shape, which is covered by four {110} facets. However, Figure 1.8 shows that the shape of the capped dots changes into a dome-like shape. After the GaAs capping, the lateral size and height were decreased. The effects depend on the strain and enhance for the larger dots having large strain.

During the capping growth of GaAs, the composition, the shape and the size of QDs were changed. The modification of the QD structure is mainly attributed to the In surface segregation and In-Ga intermixing effects during the GaAs capping growth. Therefore, such modification by the capping growth will influence the size uniformity of QDs [14]. It is possible to decrease an inhomogeneous broadening in the dot size by a proper GaAs capping growth.

The strain due to the lattice mismatch is more stored in the large InAs QDs. A large density of misfit dislocations is introduced and affects the optical and electrical properties of the QDs. Therefore, the excess compressive strain must be reduced to suppress the generation of dislocations with a GaAs capping layer above the QDs [13].

(4) Different strain-reducing layer on InAs QDs

Akahane *et al.* and Liu *et al.* have reported on lengthening of the emission wavelength of InAs QDs by introducing a strain-reducing layer (SRL) [15, 16]. GaAsSb SRL on InAs (3 ML) QDs embedded between 100 nm GaAs capping layer, which has a wavelength redshift in photoluminescence spectrum. Figure 1.9 (a) and (b) compare schematic band diagrams of two heterostructures. Capping InAs/GaAs QDs with a thin $In_{0.15}Ga_{0.85}As$ (6 nm) layer reduces the confinement potential for both electrons and holes. However, capping with $GaAs_{0.86}Sb_{0.14}$ (6 nm) provides electron confinement which is essentially identical to that obtained by using GaAs, a result of the small GaAs/GaAsSb conduction band offset. In other words, the GaAsSb SRL acts to suppress the carriers escape from QDs. Therefore, GaAsSb SRL provides a further enhancement of the QD properties.

The room temperature photoluminescence at 1.62 μm from InGaAs QDs capped with $GaAs_{0.83}Sb_{0.17}$ (8 nm) shown in Figure 1.10 has been recently reported by Ripalda *et al.* [17]. The samples were grown on GaAs (001) by solid source molecular beam epitaxy. It has used InAs (2.2 ML) as a QD seed layer, followed by $In_{0.5}Ga_{0.5}As$ (8 ML) QDs. The presence of Sb during capping of the InGaAs QDs has two major effects. One is a wavelength redshift and a broadening of the main photoluminescence peak. The maximum peak intensity of luminescence is located at a wavelength of 1.62 μm for the GaAsSb capped InGaAs QDs layer. The other is that the separate electron and hole confinement is likely to lead to long radiative recombination lifetimes, and this makes the samples more sensitive to nonradiative recombination at structural defects, such as those due to the large lattice misfit induced by Sb and In incorporation. However, enhancement of the photoluminescence intensity is needed.

(5) Different buffer materials under InAs QDs

Shimizu *et al.* investigated four types of buffer materials, in terms of GaAs, $GaAs_{0.98}Sb_{0.02}$ (7 nm), $InGa_{0.13}As_{0.87}$ (1 nm), and Si buffer [18]. The samples were grown on GaAs (001) by solid source molecular beam epitaxy.

The photoluminescence intensity decreases monotonously with the increases in the dot density for all types of buffers. The relationship between the photoluminescence intensity and the dot density is almost the same for GaAs, InGaAs, and Si buffer. However, the photoluminescence intensity increases about three times when GaAsSb buffer is used, as shown in Figure 1.11. This was attributed to the reduction of the interfacial defects of the QDs by the surfactant behavior of Sb.

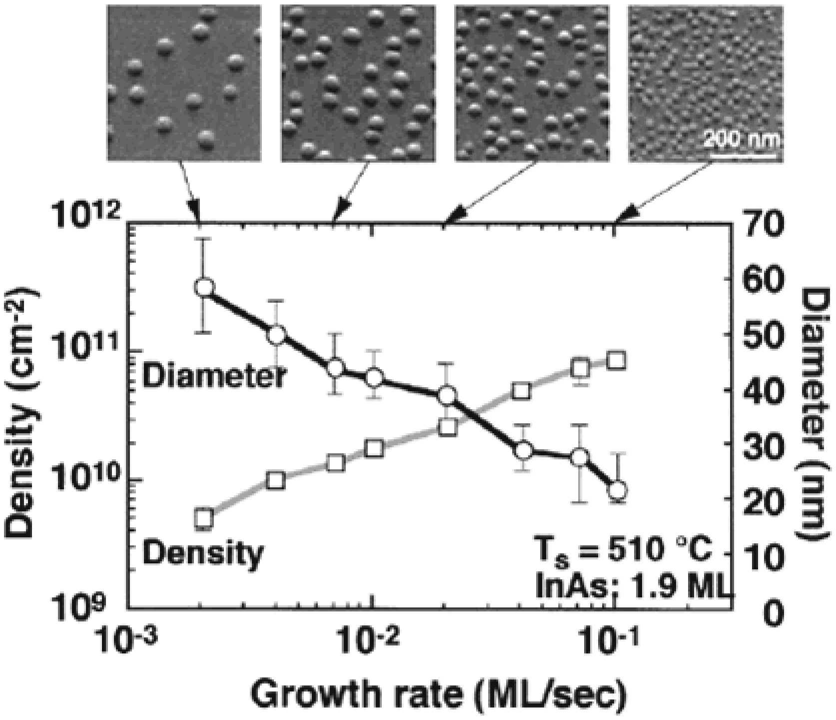

Figure 1.5 Base diameter and density of the uncapped islands measured by AFM as a function of growth rate [9].

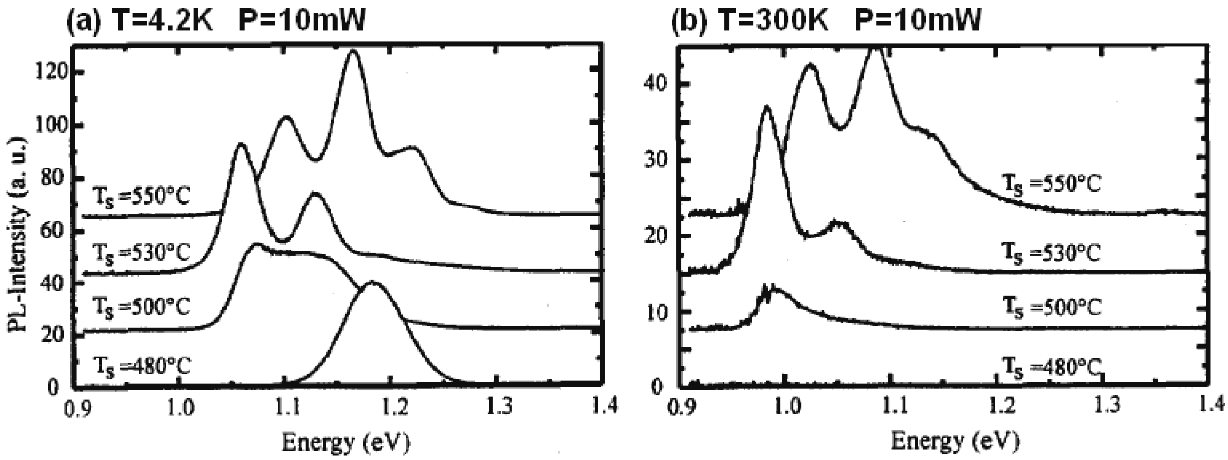

Figure 1.6 The optical properties of QDs are significantly affected by different substrate temperature. (a) 4.2 K and (b) room temperature [10].

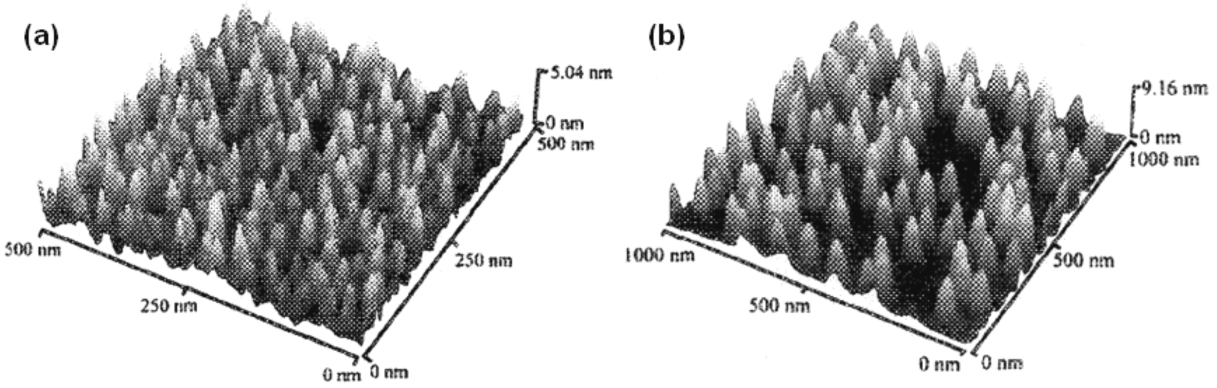

Figure 1.7 AFM images of corresponding uncapped QDs grown at (a) 480 °C and (b) 530 °C. The dots density approximately of 1×10^{11} cm^{-2} and 1.2×10^{10} cm^{-2}, respectively [10].

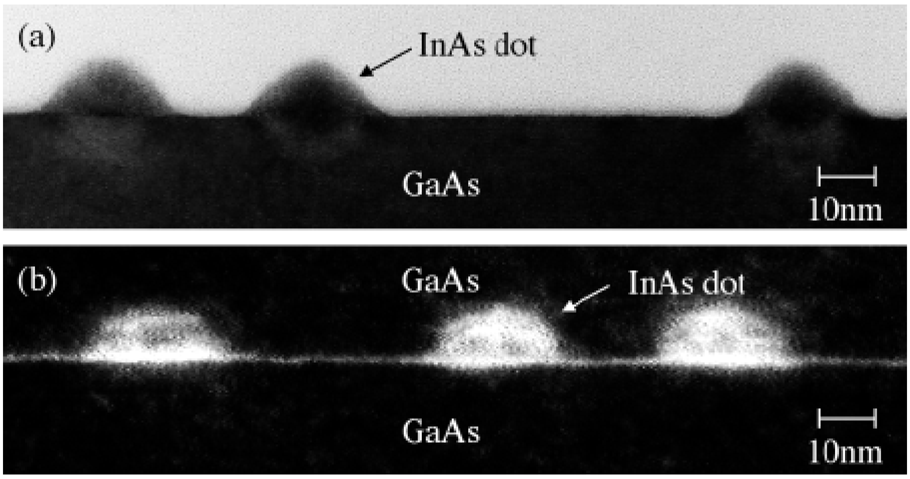

Figure 1.8 (110) cross-sectional TEM and HAADF-STEM images of (a) uncapped InAs dots and (b) InAs dots covered by GaAs layer [13].

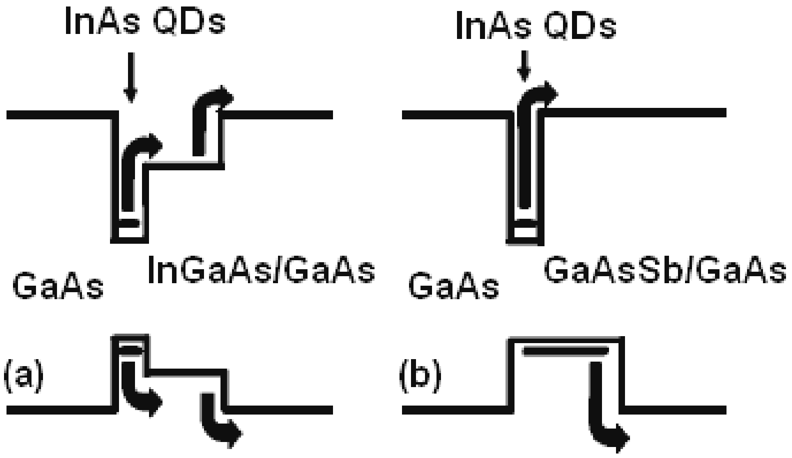

Figure 1.9 Schematic band diagrams of (a) InAs/InGaAs/GaAs and (b) InAs/GaAsSb/GaAs structures [16].

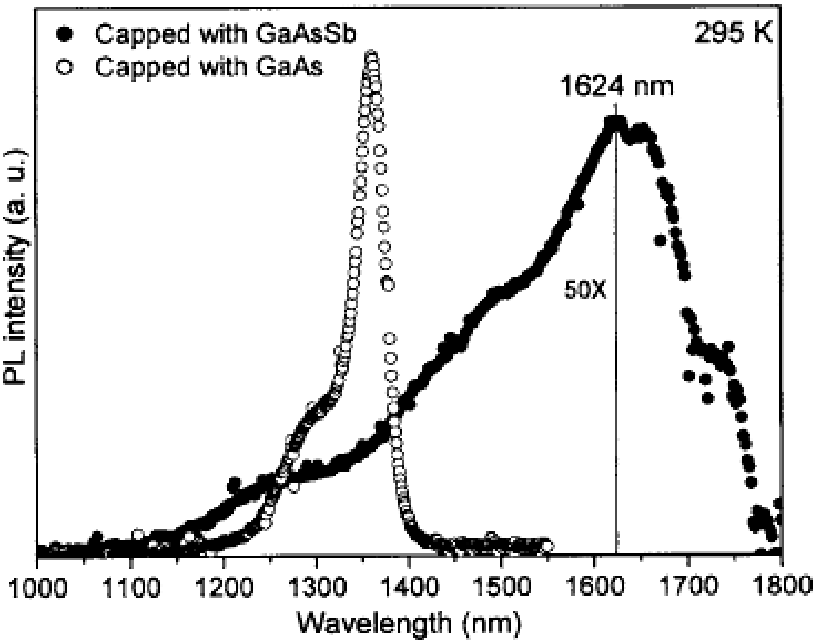

Figure 1.10 The room temperature photoluminescence spectra of GaAs and $GaAs_{0.83}Sb_{0.17}$ capped InGaAs QDs [17].

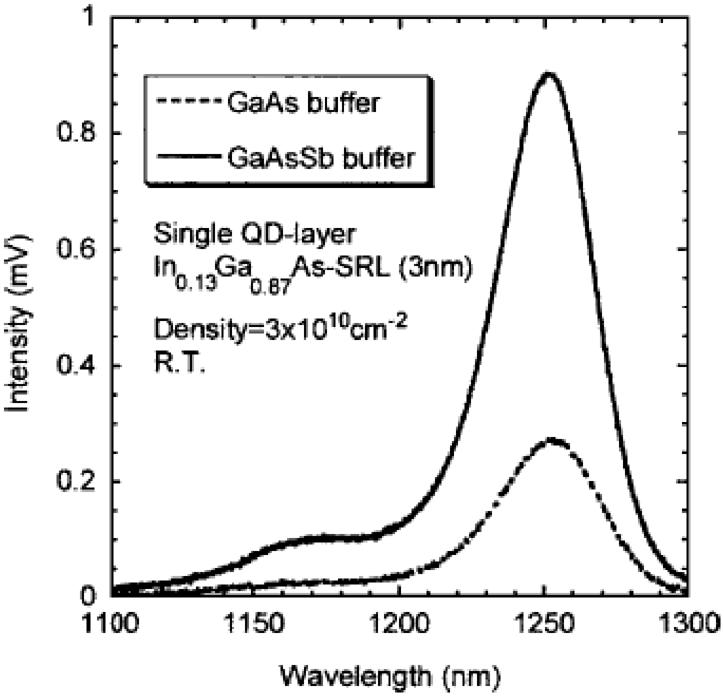

Figure 1.11 The room temperature photoluminescence spectra of GaAs and $GaAs_{0.98}Sb_{0.02}$ buffer both with the dot density of 3×10^{10} cm^{-2} [18].

1.3. Motivation

In terms of industrial applications, the use of Sb materials provides the promising production for better quantum dot lasers. The ability to tune the size of QDs is the crucial issue for development quantum dot lasers.

As Sb is known to reduce the surface energy and results in both an increase of the dots density and a suppression of coalescence [19]. It has recently been reported that QD formation can be influenced by using the Sb surfactant [20]. The exact mechanism of surfactant-mediated growth is still under debate, but the most generally reported the effect of Sb surfactant species is to lower the surface energy and to drive the growth in a diffusion-limited regime, as well as segregate to the growth front. As a result of using Sb into QD structure is probably attributed to changes of surface and interface energies [21]. However, the growth of InAs QDs on the GaAsSb buffer layer of different Sb composition remains to be studied for clarify the effect of antimony in terms of surface and lattice match. According the previous literature review, this important topic will be a focused field for further study in the future.

The motivation of this work is to explore how the Sb acts in the buffers of $GaAs_{1-X}Sb_X$ ($X = 0\%$, 5.72%, and 11.44%) on the growth of InAs QDs. Different concentrations of Sb in GaAs as a buffer layer may have a change of lattice mismatch and energy gap. Photoluminescence measurements and transmission electron microscopy were performed to investigate the optical and structural properties of QDs, and the influences of the tunable GaAsSb buffer layer on QDs will be discussed in the thesis.

Chapter 2　Sample Fabrication and Experimental Design

2.1. Molecular Beam Epitaxy Growth of InAs Quantum Dots

A promising way of self-assembled and defect free QD fabrication is SK growth in lattice mismatched systems. Molecular beam epitaxy (MBE) is one of the most commonly used methods for depositing QDs.

MBE is an ultra-high vacuum (UHV) based technique for producing high quality epitaxial structures with monolayer control. Since its introduction in the 1970s as a tool for growing high purity semiconductor films, MBE has evolved into one of the most widely used techniques for producing epitaxial layers of metals, insulators and superconductors as well, both at the research and the industrial production level. The principle underlying MBE growth is relatively simple: it consists essentially of atoms or clusters of atoms which are produced by heating up a solid source. They as a beam then migrate in an UHV environment and impinge on a hot substrate surface, where they can diffuse and eventually incorporate into the growing film. Despite the conceptual simplicity, a great technological effort is required to produce systems that yield the desired quality in terms of material purity, uniformity and interface control.

The three samples were fabricated and provided by Industrial Technology Research Institute (ITRI) in Hsinchu, Taiwan. The n^+ GaAs (001) substrates were Si doped to 1.0×10^{19} cm^{-3}. At the beginning, a 0.3-μm-thick GaAs buffer layer with Si doped to 6.0×10^{16} cm^{-3} was deposited on the substrates with a growth rate of 3 Å/s at 600 °C. Subsequently, a nominal 10 Å GaAsSb buffer layer was grown with a growth rate of 3 Å/s at 600 °C. Three different Sb composites designate as samples 1, 2, and 3 were deposited with 0% Sb, 5.72% Sb and 11.44% Sb respectively. 2.4 ML (equal to 7.2 Å) with a growth rate of 0.28 Å/s at 485 °C of InAs was deposited for the formation of QDs. The dots were self-assembled on a thin wetting layer. Finally, a 0.3-μm-thick GaAs capping layer with Si doped to 6.0×10^{16} cm^{-3} was grown on QDs with a growth rate of 3 Å/s at 600 °C. Figures 2.1 and 2.2 display the schematic view and energy gap of the three samples.

The lattice constant of GaAsSb buffer layer and the lattice mismatches for bulk materials of samples 1, 2 and 3 listed in Table 2.1. Comparing the lattice mismatch with the coverage, Figure 2.3 shows that the InAs/GaAsSb QD structure is in the region of the SK growth mode in this work.

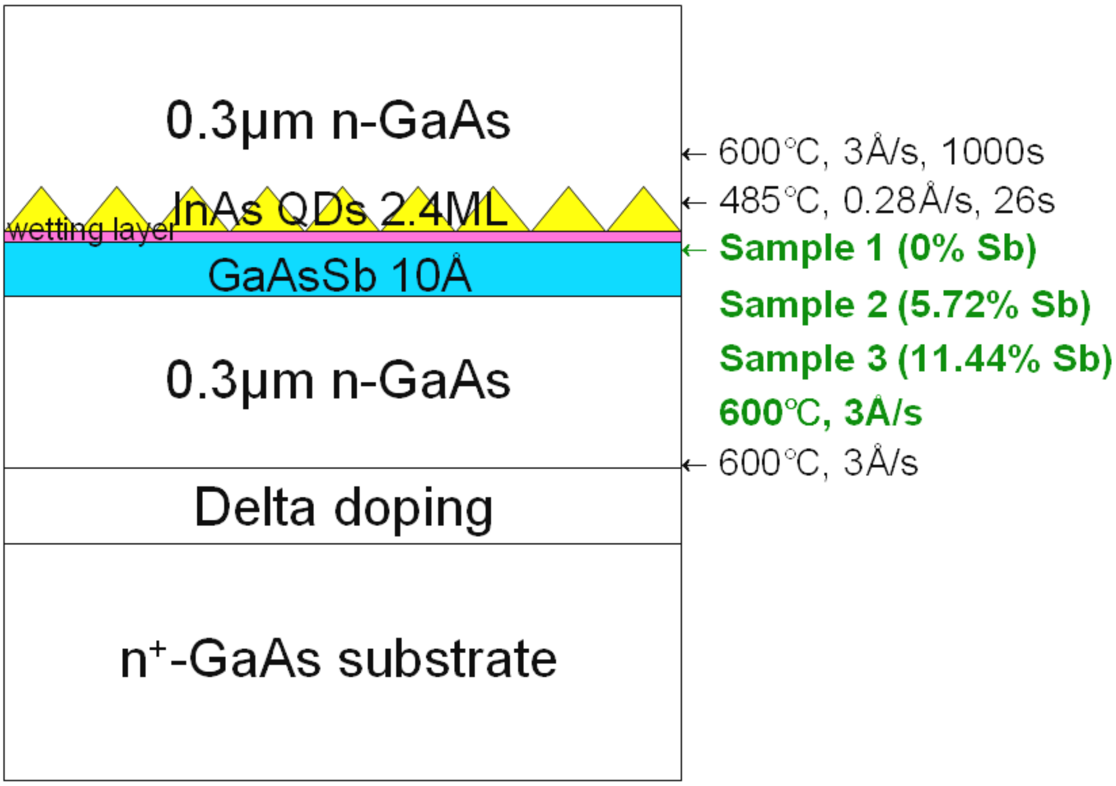

Figure 2.1 Schematic views of three samples for the structures and growth conditions.

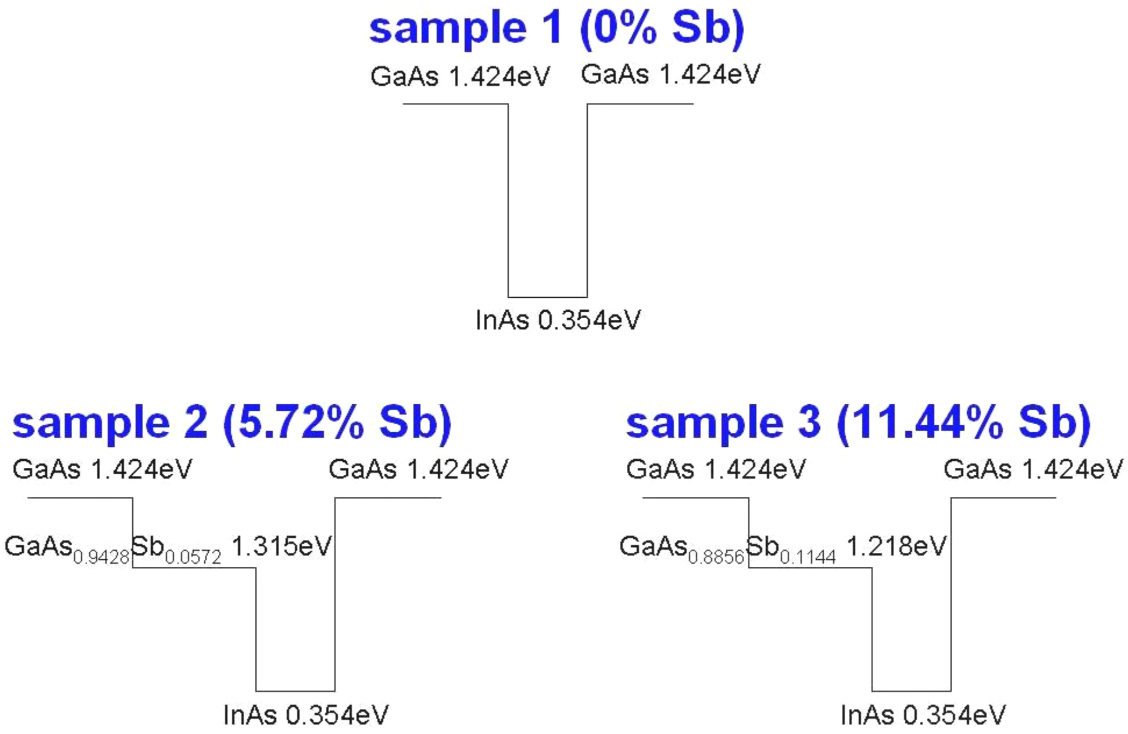

Figure 2.2 Schematic diagrams of three samples for their energy gap.

Table 2.1 For bulk materials, GaAsSb lattice constant and InAs/GaAsSb lattice mismatch of samples 1, 2 and 3, respectively.

	GaAs$_{1-X}$Sb$_X$ Lattice constant	GaAs$_{1-X}$Sb$_X$ / GaAs Lattice mismatch	InAs / GaAs$_{1-X}$Sb$_X$ Lattice mismatch
Sample 1 (0% Sb)	5.65Å	0	7.16%
Sample 2 (5.74% Sb)	5.66Å	0.13%	7.03%
Sample 3 (11.44% Sb)	5.67Å	0.25%	6.90%

$$Lattice\ mismatch = \frac{Upper\text{-}Lower}{Lower} \times 100\%$$

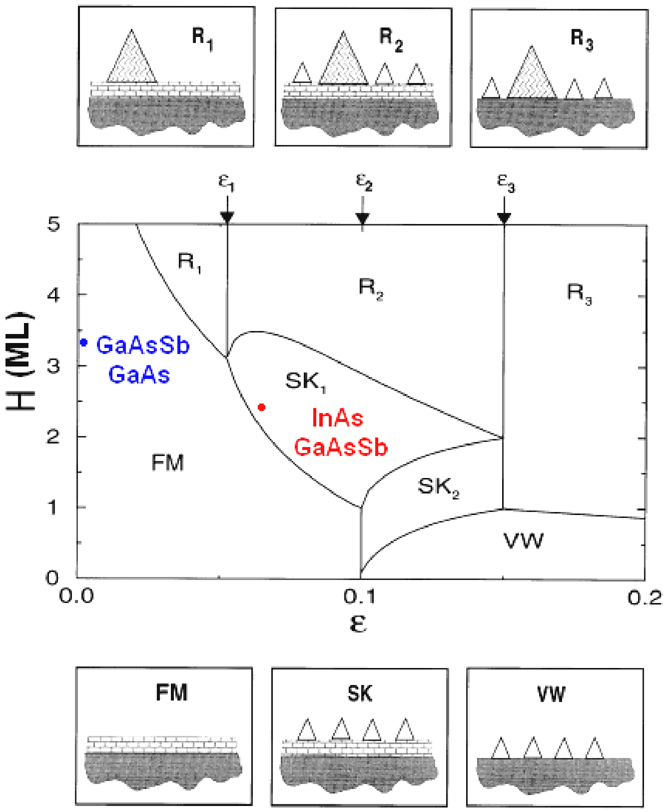

Figure 2.3 Equilibrium phase diagram in the function of the coverage H in monolayer and lattice misfit ε [22].

2.2. Analytical Techniques

The experimental design divided into three parts which were about the influence of Sb diffusion on QDs, the optical and structural properties of QDs. The study of InAs QDs structure on GaAsSb buffer layer has analyzed with secondary ion mass spectrometry (SIMS), photoluminescence (PL), transmission electron microscopy (TEM), and energy dispersive X-ray spectroscopy (EDS).

2.2.1. Secondary Ion Beam Spectroscopy

SIMS has proven to be a versatile analysis technique for measuring doping profiles of semiconductor materials and thin films because it can detect impurities and dopants at extremely low atomic concentration of less than one part per million. Simplistically, secondary ion formation can be divided into two consecutive steps: sputtering and ionization. During SIMS analysis, the sample surface is slowly sputtered away. Continuous analysis while sputtering produces information as a function of depth, called a depth profile. When the sputtering rate is extremely slow, the entire analysis can be performed while consuming less than a tenth of an atomic monolayer. This slow sputtering mode is called static SIMS in contrast to dynamic SIMS used for depth profiles. Shallow sputtering minimizes the damage done to organic substances present on the sample surface. The resulting ion fragmentation patterns contain information useful for identifying molecular species. Only dynamic SIMS will be treated in this surface analysis computer aided instruction package because the dynamic SIMS yields qualitative information [23].

Primary beam species useful in SIMS include Cs^+, O_2^+, O, Ar^+, and Ga^+ at energies between 1 and 30 keV. Primary ions are implanted and mix with sample atoms to depths of 1 to 10 nm. Sputter rates in typical SIMS experiments vary between 0.5 and 5 nm/s. Sputter rates depend on primary beam intensity, sample material, and crystal orientation. The sputter yield is the ratio of the number of atoms sputtered to the number of impinging primary ions. Typical SIMS sputter yields fall in a range from 5 and 15.

The secondary ion counts from SIMS measurements can be quantified to atomic concentration in reasonable accuracy by relative sensitivity factors for typical impurity elements in GaAs materials. These SIMS depth profiles provide valuable information for the development of semiconductor epitaxial structures and the analysis of device performance. Therefore, the depth profile of Ga, As, In and Sb concentration measured by SIMS in the QD structures for characterization of Sb distribution because of its low quantity of volume within the structure [24].

In this study, the SIMS data were accomplished and at the Instrument Center of National Science Council at National Tsing Hua University. SIMS analysis was performed with a magnetic-sector Cameca IMS-4f spectrometer equipped with O_2^+, O*, and Cs^+ ion sources. It was sputtered with Cs^+ beam ions of 1 keV and 40 nA, a sputtering area of 250×250 μm^2, and analyzed with ^{69}Ga ion gun.

2.2.2. Photoluminescence

PL, where light separates charge carriers within the band or impurity structure of a semiconductor, whose later recombination produces characteristic emissions. PL includes fluorescence as well as phosphorescence. Respectively, fluorescence and phosphorescence are given the definition of the radiative transition is a spin-allowed transition between two states with equal multiplicity and a spin-forbidden transition between two states with different multiplicities. In general, fluorescence lifetimes (10^{-10}~10^{-8} s) are much shorter than phosphorescence lifetimes (10^{-3}~10 s), and thus fluorescence has also been defined as PL which occurs promptly after excitation, while phosphorescence is discernibly delayed. Because of its high sensitivity and selectively, fluorescence spectrometry has been used for years as a major analytical tool in research [25].

A photon whose energy equals or exceeds the gap value can excite a valence electron across the gap. Absorption also occurs when the photon raises an electron from a neutral donor to the conduction band or from the valence band to a neutral acceptor. It is also possible to induce absorptive transition from the valence band to an ionized donor or from an ionized acceptor to the conduction band. The processes are fruitful probes of semiconductor bands and impurities. They also lead to the more sensitive probe of PL, which occurs when excited electron returns to its initial state.

The fundamental luminescence processes are divided into three steps. First, an electron is excited from the valence band to conduction band. Second, the nonequilibrium electron and hole distributions tend to relax back into the ground state. Finally, the electron-hole pairs recombine with emission of light which is the PL process [26]. This can proceed in either radiative or non-radiative form. Radiative processes include the radiative recombination or collapse of an exciton, and the involvement of a recombination center. Non-radiative forms include the Auger process, a three-carrier phenomenon which may also involve a recombination center; and multiphonon processes, which may also involve defect sites. It is of course the radiative recombination which is observed in PL spectroscopy; but the non-radiative processes are competing elements, which if too strong may prelude PL. Hence different types of process produce different characteristic PL peaks and distributions [27].

PL is one of the most useful optical methods for the semiconductor industry, with its powerful and sensitive to find impurities and defects in silicon and group Ⅲ-Ⅴ semiconductors, which affect materials quality and device performance.

In this study, the PL experiments were accomplished at the Department of Electrophysics at National Chiao Tung University. The 532 nm line from an Ar$^+$ solid-state laser was used as the excitation source in the PL measurements. The luminescence signal was dispersed by a triple-grating monochromator and detected by an InGaAs photodetector. The resolution was about 2.2 nm. The detector signal was amplified with a standard lock-in technique. PL measurements were carried out in the temperature range of 20~300 K with the excitation power varying from 1.3 μW to 1.3 W.

2.2.3. Transmission Electron Microscopy

As the electrons travel through a very thin specimen, they are either scattered by a variety of processes or they may remain unaffected by the specimen. The end result is that a nonuniform distribution of electrons emerges from the exit surface of the specimen. It is this nonuniform distribution that contains all the structural and chemical information about the specimen. Electron scattering can be grouped in two ways, that are elastic and inelastic scattering. There terms are simply descriptions of scattering that result in no loss of energy and some measurable loss of energy, respectively. Elastically scattered electrons are the major source of contrast in TEM images and they also create the intensity in diffraction patterns

(DPs). Inelastic scatter transfers energy to the specimen, generating a lot of useful signals which form different images of the specimen or get spectroscopic information about its chemistry and electronic structure.

The uniform electron intensity in the incident beam is transformed into a nonuniform intensity after scattering by the specimen. The variable electron intensity hits the viewing screen or the electron detector, which translates into contrast on the screen. That is DP shows nonuniformity because it separates out the diffracted and direct beams. Therefore, a fundamental principle of imaging in the TEM is [28]: first view the DP, since this pattern tells about the scattering of the specimen. DPs are the basis of all image formation in the TEM as all crystallographic analysis and defect characterization. In order to obtain a DP with a parallel with beam of electrons, the stander way is to use a selecting aperture. This operation is called selected-area diffraction (SAD). By selecting the direct beam and the diffracted beam in SAD pattern to form bright field (BF) and dark field (DF) images, respectively. To get good strong contrast in both BF and DF images, it is necessary to tilt the specimen to two-beam conditions in which the diffracted beam and the direct beam, are only the two strong spots in the pattern.

TEM image contrast arises because of the scattering of the incident beam by the specimen. The electron wave can change both its amplitude and its phase as it traverses the specimen and both these kinds of change can give rise to image contrast. Thus a fundamental distinction in TEM is between amplitude contrast and phase contrast. The amplitude contrast that there are two principal types, namely mass-thickness contrast and diffraction contrast. Mass-thickness contrast is most important in looking at amorphous materials such as polymers. Diffraction contrast from regions close to the defect would depend on the properties of the defect, the strain field especially. Phase contrast imaging is often thought to be synonymous with high-resolution TEM (HRTEM) [28]. In fact, phase contrast appears in most TEM images even at low magnifications. Phase contrast can be exploited to image the atomic structure of a thin specimen.

Buried dots have been analyzed principally by high-angle annular dark field-scanning transmission electron microscopy (HAADF-STEM) of cross-sectional specimens. The size of QDs can be estimated from the contrast, whereas the composition is much more difficult to qualify, since the contrast is weak and the strain sensitivity in electron microscopy is insufficient for the level of precision required. Most TEM equipped with EDS and electron energy loss spectrometry (EELS), giving the chemical information and a lot of other detail about the samples. An estimate of the composition can be made by combining STEM using a very small probe with EDS, however EDS cannot provide an absolute composition value and since STEM creates a two-dimensional image of the dot assumptions are need regarding the dot shape [29]. Furthermore, HRTEM can be used to determine the morphology of QD, the local strain and structural peculiarities on atomic scale.

In this work, TEM (JEOL JEM-2010F) studies were performed on the magnification from 2000 to 1500000 at 200 kV with a filed emission gun in National Device Laboratories (NDL). It was also equipped with STEM, EDS, EELS and CCD cameras.

Electron microscopy imaging is the only direct method of structural investigation with sufficient resolution for capped QDs without destroying the buried dots [30]. Among these the cross-sectional and the plan-view TEM imaging techniques are suitable methods to characterize directly the shape, the size, and the strain field of nanometer-scaled structures and related defects, especially using electron diffraction contrast imaging with BF and DF modes. DF images using the 200 diffraction condition are frequently used [31], viewing the layers edge-on in a cross-sectional specimen. The contrast of bright and black regions in TEM image has its origin in the well-know composition sensitively of the 200 reflection [32]. It can use the structure factor to interpret the chemical sensitive for the 200 reflection and strain sensitive for the 400 reflection. The scattering from the unit cell by the expression

$$A_{\text{cell}} = \frac{e^{2\pi ikr}}{r} \sum_i f_i(\theta) e^{2\pi i\mathbf{K}\cdot\mathbf{r}_i}$$

What this equation says is that the atoms within the unit cell all scatter with a phase difference given by $2\pi i\mathbf{K}\cdot\mathbf{r}_i$ where $\mathbf{r}_\text{i}$ is a vector which defines the location of each atom within the unit cell [28]

$$\mathbf{r}_i = x_i\mathbf{a} + y_i\mathbf{b} + z_i\mathbf{c}$$

By considering only the case where **K** = **g** since this is an infinite, perfect cell

$$\mathbf{K} = h\mathbf{a}^* + k\mathbf{b}^* + l\mathbf{c}^*$$

So, the structure factor function can be written

$$F_{hkl} = \sum_i f_i e^{\frac{\pi}{2} i\,(h+k+l)}$$

For face-centered cubic (fcc), the coordinates of atoms are

$$(\text{x}, \text{y}, \text{z}) = (0, 0, 0), (\frac{1}{2}, \frac{1}{2}, 0), (\frac{1}{2}, 0, \frac{1}{2}), (0, \frac{1}{2}, \frac{1}{2})$$

Substituting these values into $\mathbf{r}_\text{i}$ the above equation gives

$$F_{\text{fcc}} = f\,\{1 + e^{\pi i\,(h+k)} + e^{\pi i\,(h+l)} + e^{\pi i\,(k+l)}\}$$

$$\begin{aligned} F_{\text{fcc}} &= 0 && \text{if } h, k, l \text{ are mixed even and odd.} \\ F_{\text{fcc}} &= 4f && \text{if } h, k, l \text{ are all even or all odd.} \end{aligned}$$

For GaAs materials, the Ga located on the fcc lattice and the As related to it by the basis vector [1/4, 1/4, 1/4]. The expression for F becomes

$$F = \{f_{\text{Ga}} + f_{\text{As}} e^{\frac{\pi}{2} i\,(h+k+l)}\}\, F_{\text{fcc}}$$

$$\begin{aligned} F &= 4\,(f_{\text{Ga}} - f_{\text{As}}) && \text{if } h, k, l \text{ are all even and } h+k+l = 2N \\ & && \text{where } N \text{ is odd (e.g., the 200 reflection).} \\ F &= 4\,(f_{\text{Ga}} + f_{\text{As}}) && \text{if } h, k, l \text{ are all even and } h+k+l = 2N \\ & && \text{where } N \text{ is even (e.g., the 400 reflection).} \end{aligned}$$

The intensity is equal to the square of amplitude (i.e., F^2), so the intensity is present

$$I = |A|^2 = F_{(200)}{}^2 = 16\,(f_{\text{Ga}}{}^2 - f_{\text{As}}{}^2)$$

$$I = |A|^2 = F_{(400)}{}^2 = 16\,(f_{\text{Ga}}{}^2 + f_{\text{As}}{}^2)$$

The atomic scattering factor $f(\theta)$ of Ga and As are given

$$f_{\mathrm{Ga}} = 3.64 \qquad f_{\mathrm{As}} = 4.07$$

Therefore, the intensity of the 400 reflection is larger than the 200 reflection.

The 200 and 400 reflections are both sensitive to the chemical composition of InAs/GaAs QD structures. However the intensity of the {200} beam is smaller than that of the {400} beam, a typical DP of a QDs layer is shown in Figure 2.4. Consequently, the 400 diffraction condition is chosen to form the DF image in this study.

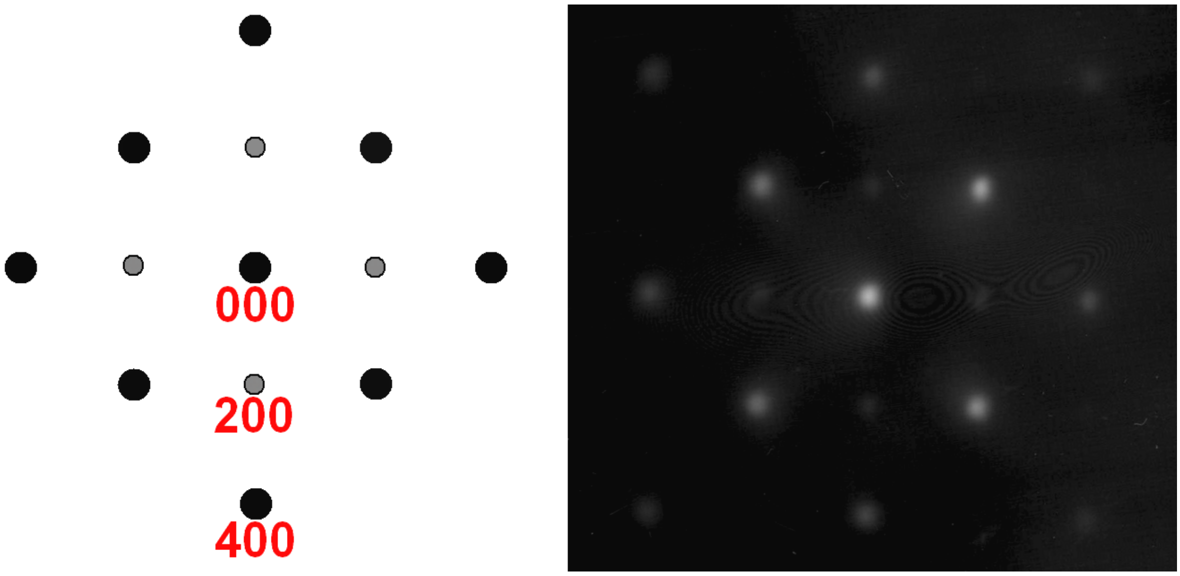

Figure 2.4 The schematic diagram (left panel) and the TEM image (right panel) of DP for InAs/GaAs QD structures.

2.3. Preparation of TEM Specimens

The requirement for thin specimen is a major limitation of the TEM. For a specimen to be transparent to electrons it must be thin enough to transmit sufficient electrons such that enough intensity falls on the screen or photographic film to give an interpretable image in a reasonable time. Generally this requirement is a function of the electron energy and the average atomic number of the specimen. It is an axiom in TEM that a thinner specimen is a better way and easily to get successful results.

2.3.1. Plan-view TEM Specimens

(1) The 2×2 mm specimen is adhered on the supporter with the upside to the bottom of specimen, and four pieces of dummy of Si are surrounded with the specimen, as shown in Figure 2.5 (a). The dummy Si has to have a suitable thickness as a criterion.

(2) Grind the specimen by means of SiC grinding paper from smaller number to larger number, followed by using diamond lapping film from 30 μm to 0.5 μm. When Si is pervious to light and then the specimen is done. Finally, polish the specimen with alumina slurry for three times.

(3) A 2 mm Mo hole grid is adhered to the specimen with super fast epoxy. The reason for using Mo grid in stead of using Cu hole grid is to avoid the contamination of Cu caused by ion milling.

(4) In order to make sure that the specimen is tightly bound with the Mo hole grid, so that the specimen is placed for one day. After that, use acetone to clean the hot mounting wax and alcohol to clean the oil sludge.

(5) A Gatan's precision ion polishing system (PIPS) which combines high powered ion guns (4 keV) and a low angle incidence (3.5º~4º) is used to thin the specimen with minimum surface damage and heating. The specimen must be carefully checked from time to time during the milling stage to see if it can be observed in the TEM. Usually, with ion milling the specimen and then observe it in the TEM back and forth until the QDs are visible clearly.

2.3.2. Cross-sectional TEM Specimens

(1) Due to the fragile characteristic of GaAs, it would better to grind the GaAs substrates with the preparing method of plan-view specimen at first. The cross-sectional specimen is prepared along <100> direction with the 3×2 mm area. So we grind the specimen in the direction of the bottom GaAs substrates to top. The target of specimen thickness is about the diameter of 50~100 μm.

(2) Subsequently, the specimen is sandwiched in between four pieces of Si with epoxy bond, as shown in Figure 2.5 (b). The specimen is fixed with binders and it is heated on a hot plate for 40~60 minutes.

(3) Adhere the specimen on the supporter and follow the forementioned steps (2)~(5) for preparing the plan-view specimen.

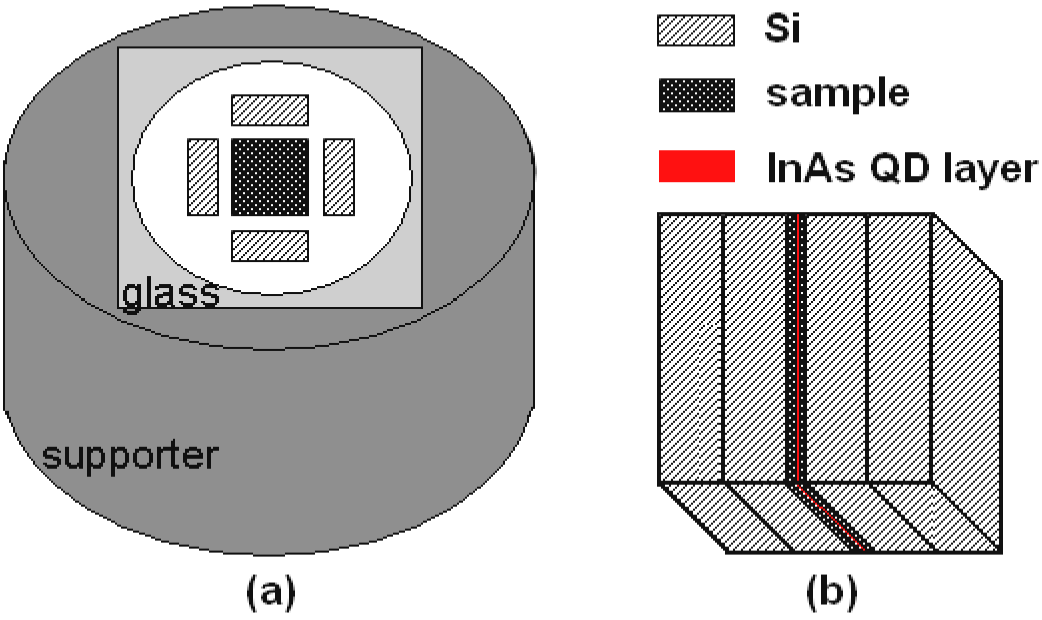

Figure 2.5 Schematic diagrams of (a) plan-view specimen on the supporter and (b) cross-sectional specimen.

Chapter 3 Results and Discussion

3.1. SIMS

The diffusion simulation indicates the atomic diffusion of Ga, As, In and Sb between GaAsSb buffer layer and InAs QDs layer. Therefore, this simulation is helpful to realize if Sb influences the formation of QDs or not. Assuming the interdiffusion process obey Fick's second law of diffusion. Wang *et al.* obtained a general solution for a single quantum well as following [33].

$$C(z) = C_2 - \frac{(C_2 - C_1)}{2}\left\{ erf\left(\frac{L_z + 2z}{4L_d}\right) + erf\left(\frac{L_z - 2z}{4L_d}\right)\right\}$$

- C_1 : the initial concentrations of atom in the well
- C_2 : the initial concentrations of atom in the barrier
- L_Z : the initial well width before interdiffusion
- $L_d = (Dt)^{1/2}$: the diffusion length, D is interdiffusion coefficient
  - $D_{In\text{-}Ga} = 5.1\times10^{-12}\exp(-1.08\ eV/kT)\ cm^2s^{-1}$ [34]
  - $D_{As\text{-}Sb} = 2\times10^{-14}\exp(-0.62\pm0.15\ eV/kT)\ cm^2s^{-1}$ [35]
- T = 600 °C, t = 1000 s

Theoretically, in the group-Ⅲ interdiffusion, Ga atoms diffuse into the QD while In atoms diffuse out. While in the group-Ⅴ interdiffusion, Sb atoms diffuse into the QD and As atoms diffuse out.

In this study, calculating with the above equation, the diffusion length between In-Ga and As-Sb are 0.546 nm and 0.268~1.97 nm, respectively. The calculations suggest that the atomic interdiffusion between QDs and buffer layer may occur within very few MLs which can alter the function of QDs and their properties.

In order to measure the element distribution of the QDs buried under the GaAs capping layer. The capping layer was removed around 150 nm by selective wet chemical etching in a solution that dissolved GaAs instead of InAs. This procedure can diminish the effect of ion mixing and the surface roughness during SIMS sputtering. The corrosive solution was composed of the proportion of $H_2SO_4 : H_2O_2 : H_2O = 1 : 1 : 100$.

Figures 3.1, 3.2 and 3.3 show that SIMS depth profiles of samples 1, 2 and 3. The depth profiles reveal that most of Sb atoms are resident roughly in the range of the QDs layer, wetting layer and buffer layer. In the continuous sputtering process, the memory effect may cause the accumulation of In and Sb atoms in the detector. As a result, the memory effect can result in broader distribution of In and Sb than the original thickness of In and Sb layer. As the sputtering effect and the depth resolution of SIMS is greater than 1~2 nm, the results can not tell anything about the Sb diffusion into InAs QDs. However, the SIMS data support the results of simulation for the range of Sb diffusion.

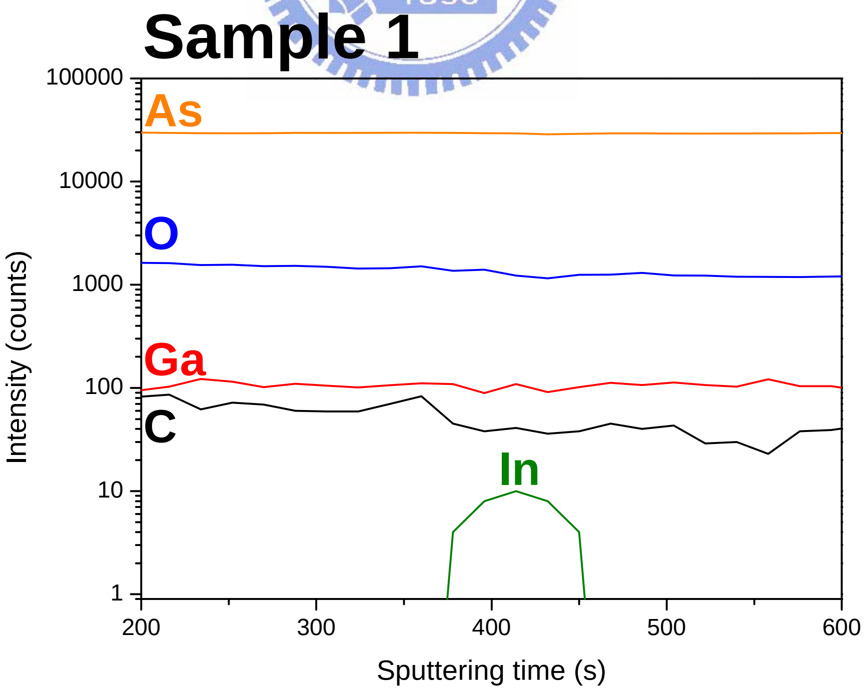

Figure 3.1 SIMS depth profile of sample 1 (0% Sb) in the QD structures.

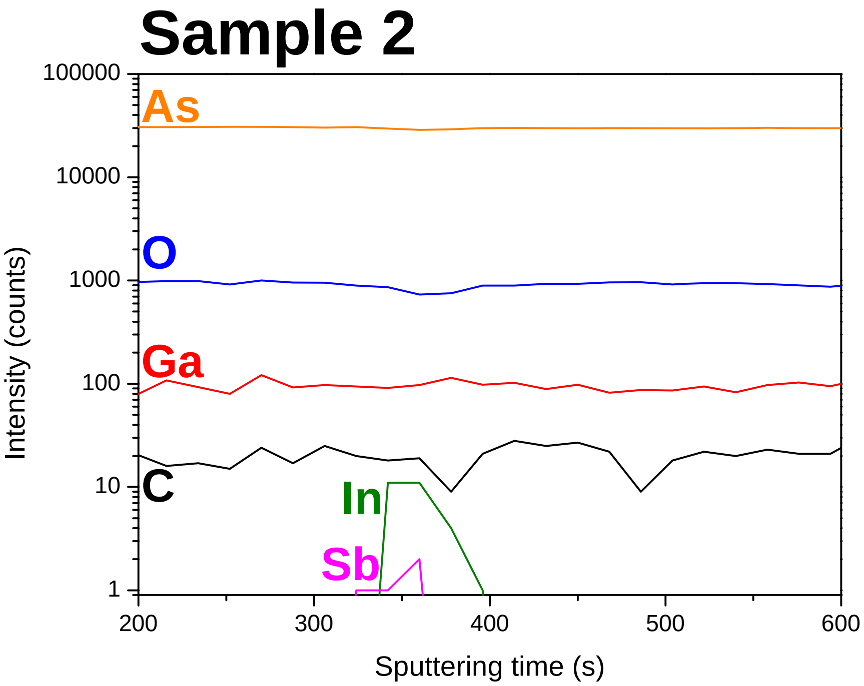

Figure 3.2 SIMS depth profile of sample 2 (5.72% Sb) in the QD structures.

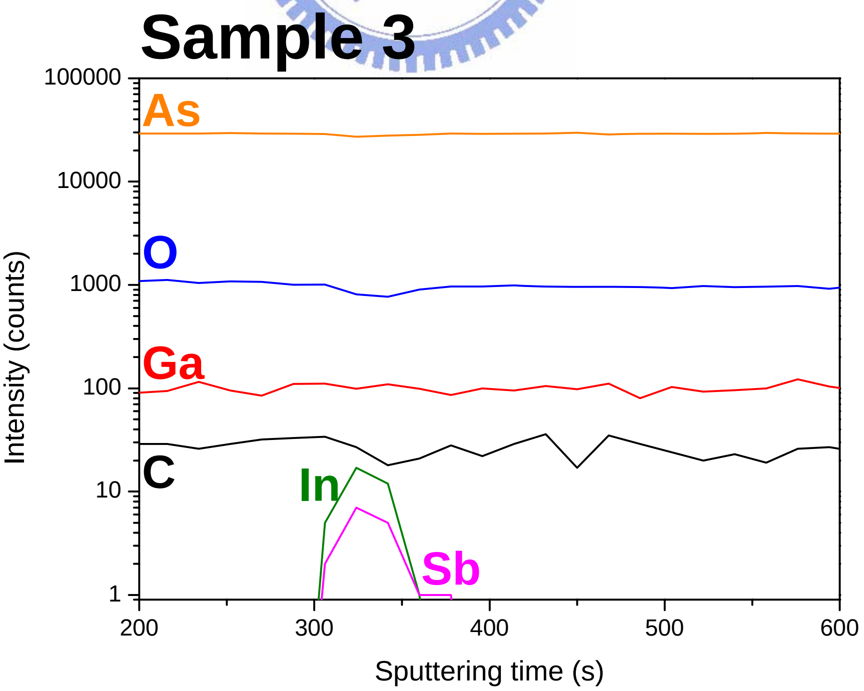

Figure 3.3 SIMS depth profile of sample 3 (11.44% Sb) in the QD structures.

3.2. PL

The optical properties of the self-assembled QDs are characterized using PL. Valuable information can be obtained from PL spectra: the PL intensity shows the optical quality, the PL energy is sensitivity to the size and composition, the full width at half maximum (FWHM) reflects the size distribution of the QDs.

The formation of self-assembled QDs is driven by the strain in lattice mismatched semiconductor materials in the heteroepitaxy. Lengthening the emission wavelength of the InAs QDs can be controlled by reducing the lattice mismatch between InAs QDs layer and GaAsSb buffer layer.

3.2.1. Power-Dependence

It has been found that the PL intensity depends on the excitation power. When the excitation power is increased, the ground state (GS) intensity rises and luminescence from the excited state (ES) can be observed, as shown in Figures 3.4, 3.5 and 3.6 for samples 1, 2 and 3 with different excitation powers.

Figures 3.7 and 3.8 display the PL spectra of three samples with 1.3 and 65 mW excitation powers at room temperature. The peak positions and FWHMs are identified by the Gaussian fitting. With the two different excitation powers, sample 2 (5.72% Sb) has the longest wavelengths of the GS and ES. It reflects that sample 2 may have the lager QDs.

Figures 3.9 and 3.10 illustrate while the excitation power increases from 1.3 to 65 mW, the emission peaks have a blueshift of wavelength and an increased FWHM in the GS and ES. In general, the larger QDs have a lower dots density than the smaller ones. With an increased concentration of Sb, the FWHMs increase of samples 2 and 3 which have a broad size distribution. Table 3.1 depicts the wavelength and FWHM in the GS and ES of samples 1, 2 and 3 with 1.3 and 6.5 mW excitation powers at room temperature. The issue about the wavelength of sample 3 is longer than sample 1 but shorter than sample 2 will discuss later.

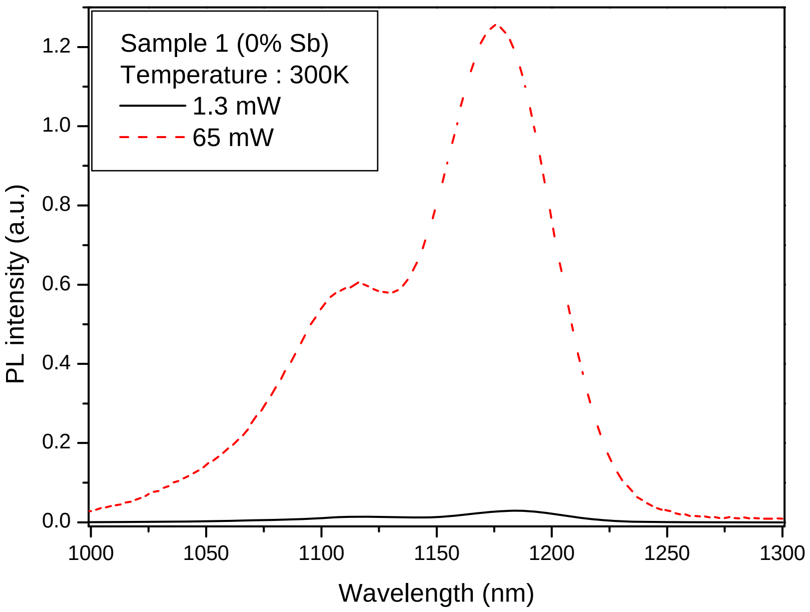

Figure 3.4 Excitation power dependent PL spectra from sample 1 at room temperature.

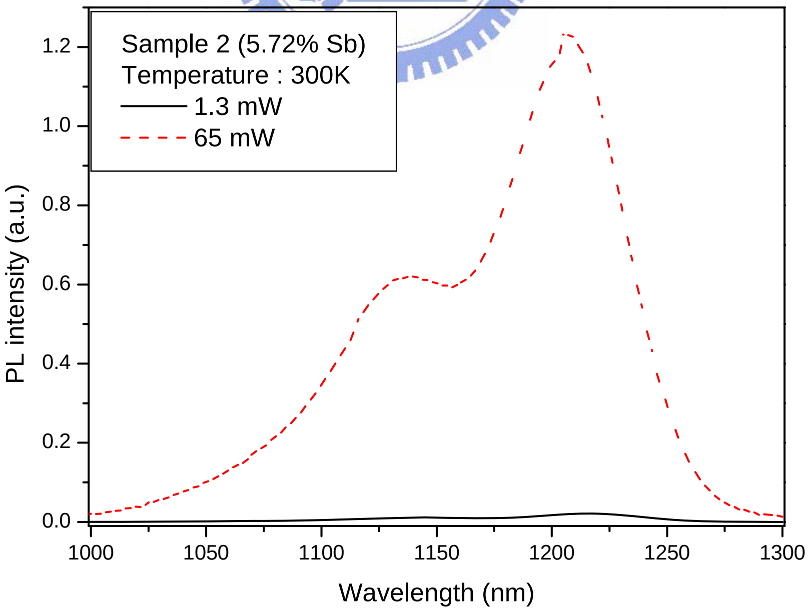

Figure 3.5 Excitation power dependent PL spectra from sample 2 at room temperature.

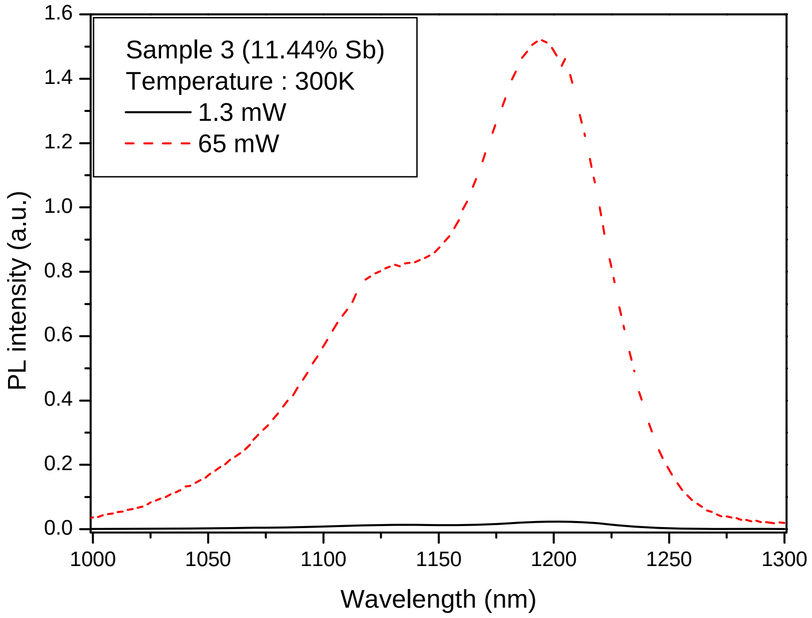

Figure 3.6 Excitation power dependent PL spectra from sample 3 at room temperature.

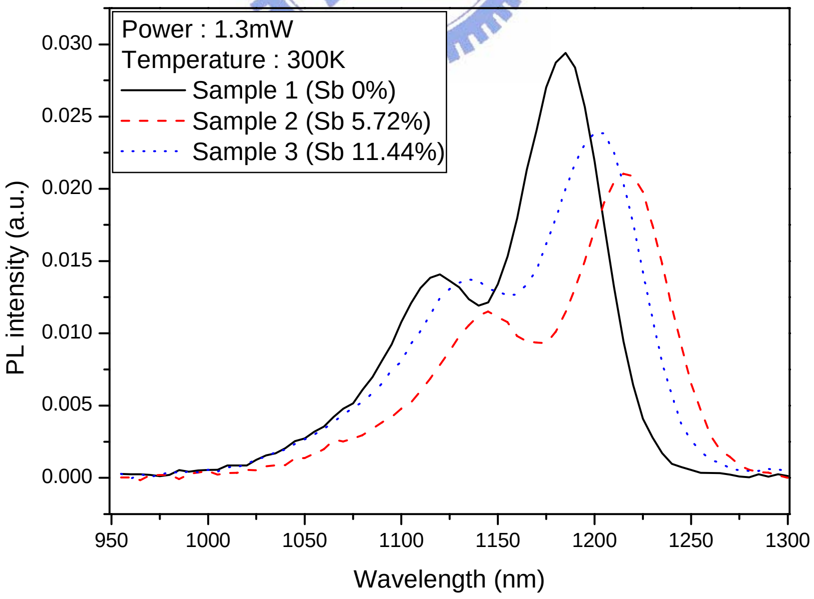

Figure 3.7 PL spectra from InAs/GaAs$_{1-X}$Sb$_X$ (X = 0, 0.0572, and 0.1144) QD structures with 1.3 mW excitation power at room temperature.

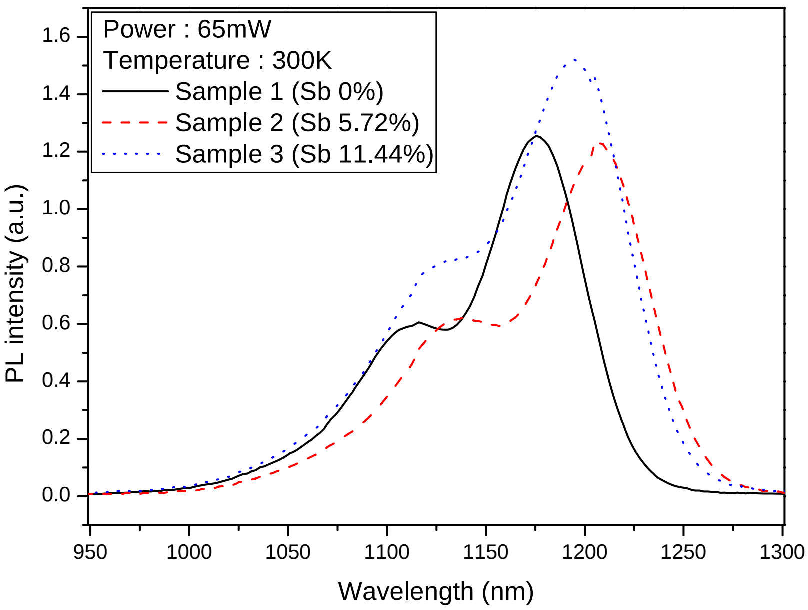

Figure 3.8 PL spectra from InAs/GaAs$_{1-X}$Sb$_X$ (X = 0, 0.0572, and 0.1144) QD structures with 65 mW excitation power at room temperature.

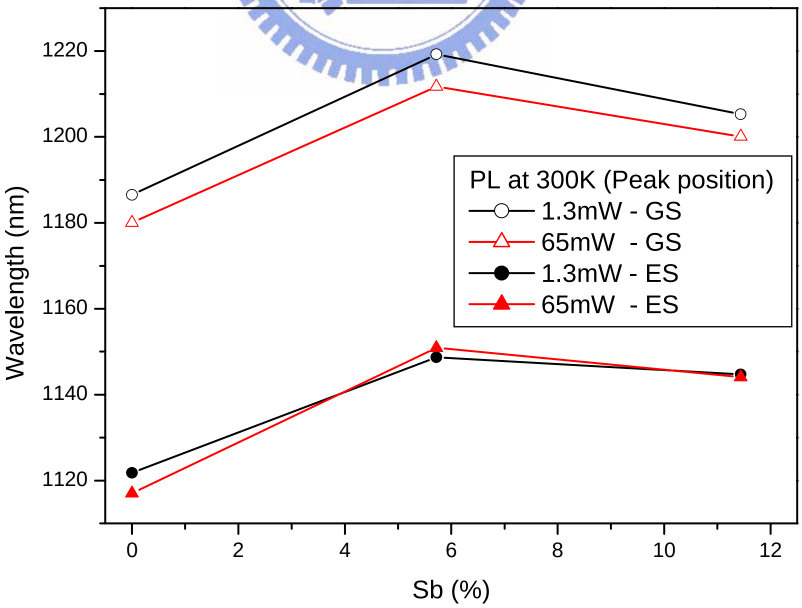

Figure 3.9 The wavelength of PL peaks in the GS and ES with 1.3 and 65 mW excitation powers at room temperature as a function of Sb concentration in the buffer layer.

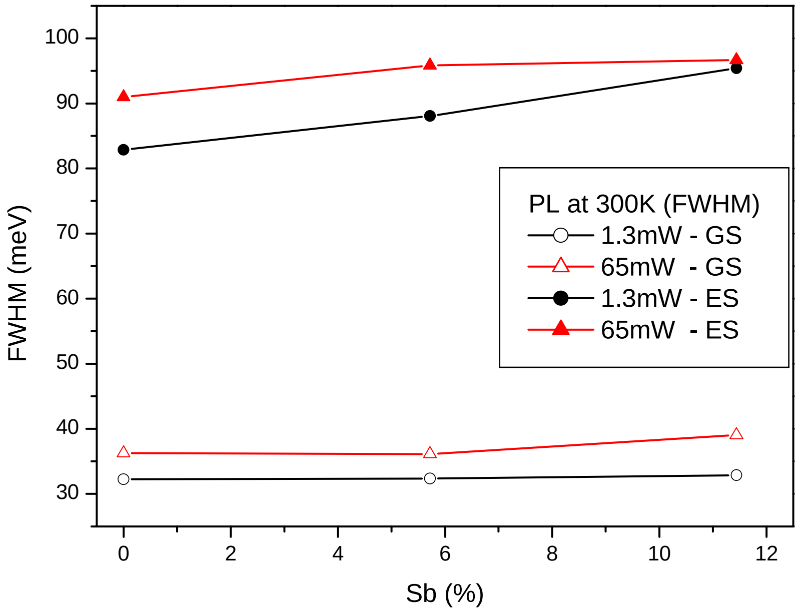

Figure 3.10 The FWHM of PL peaks in the GS and ES with 1.3 and 65 mW excitation powers at room temperature as a function of Sb concentration in the buffer layer.

Table 3.1 The wavelength and FWHM in the ground state and excited state with 1.3 and 65 mW excitation powers at room temperature of three samples.

		Excitation power 1.3 mW		Excitation power 65 mW	
		GS	ES	GS	ES
Sample 1	Wavelength (nm)	1187	1122	1180	1117
(0% Sb)	FWHM (meV)	32.25	82.87	36.26	90.99
Sample 2	Wavelength (nm)	1219	1149	1212	1150
(5.72% Sb)	FWHM (meV)	32.37	88.06	36.13	95.85
Sample 3	Wavelength (nm)	1205	1145	1200	1144
(11.44% Sb)	FWHM (meV)	32.88	95.39	39.04	96.68

3.2.2. Temperature-Dependence

At low temperatures, the transition of carriers is difficult to take place so that it can eliminate the thermal effect and improve the confinement. In another way, the carriers get extra thermal energy and result in transition at high temperatures. The low temperature PL spectra also show a smoother curve than the high temperature ones. Figures 3.11, 3.12 and 3.13 present the temperature-dependent PL spectra for samples 1, 2 and 3. For all the samples, with the increasing temperatures, the overall PL integrated intensity decreases and all spectra show a typical redshift to PL peak positions, which is mainly due to the thermal expansion of lattice [36].

Figures 3.14 and 3.15 show that the wavelength and FWHM of PL peaks in the GS and ES with 0.13 mW excitation power as a function of temperature. The fast redshift of PL wavelength and the anomalous decrease in FWHM with the increasing temperature have been attributed to the efficient relaxation process of carriers from carrier thermionic emission [37]. Figure 3.14 indicates the wavelength of the GS and ES of doping Sb in the buffer layer is longer than the sample of without doping Sb. Comparing the power-dependent PL spectra with temperature-dependent show that sample 2 (5.72%) in both types of spectra has the longest emission wavelength of the GS and ES. According to this performance of temperature-dependent PL spectra, the emission wavelength for QDs has a significant redshift in doping Sb into the buffer layer.

Figure 3.15 exhibits the FWHM of GS for three samples is almost the same. The FWHM of the ES of sample 2 is roughly increasing with the increasing temperature, but samples 1 (0% Sb) and 3 (11.44% Sb) are not. At the temperature range of 20~300 K, sample 3 has the larger FWHM value than the other two samples, which is more inhomogeneous in size distribution.

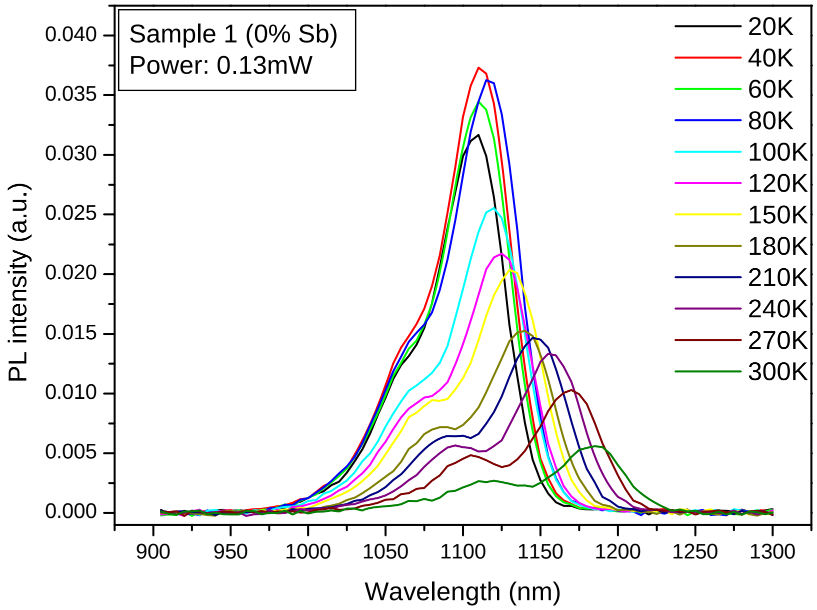

Figure 3.11 PL spectra of sample 1 with 0.13 mW excitation power at variable temperatures.

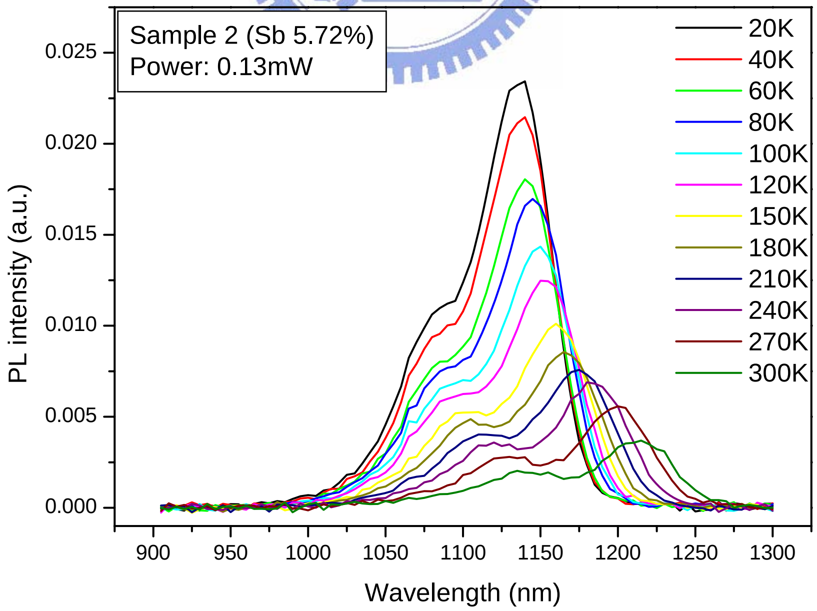

Figure 3.12 PL spectra of sample 2 with 0.13 mW excitation power at variable temperatures.

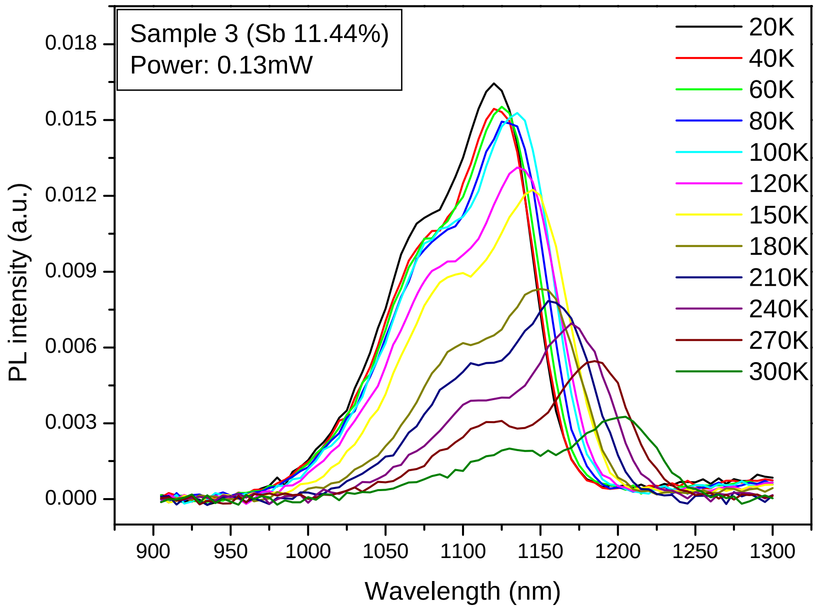

Figure 3.13 PL spectra of sample 3 with 0.13 mW excitation power at variable temperatures.

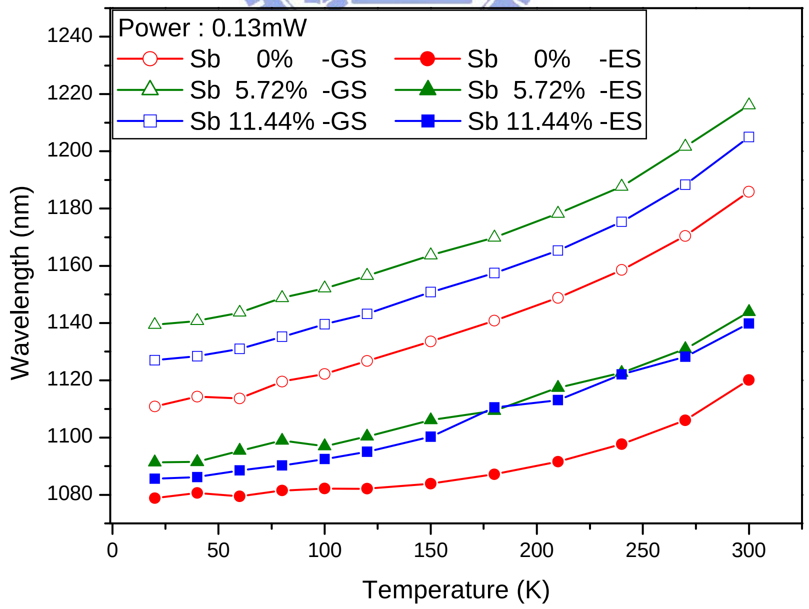

Figure 3.14 The emission wavelength of PL peaks in the GS and ES with 0.13 mW excitation power as a function of temperature.

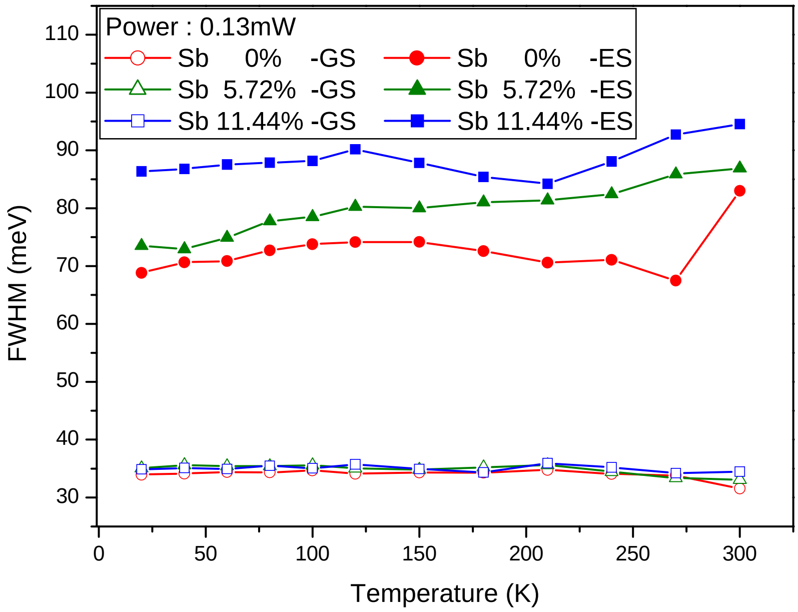

Figure 3.15 The FWHM of PL peaks in the GS and ES with 0.13 mW excitation power as a function of temperature.

3.3. Cross-sectional TEM

Figures 3.16, 3.17 and 3.18 are zone-axis BF images taken from cross-sectional specimens of samples 1, 2 and 3 at the same magnification of 150,000×. The BF TEM images are helpful to estimate the size of QDs. In BF images, notice there is a white line across the QDs of no contrast which corresponds to the plane that is without distortion by the strain field of QDs. The dark regions are induced by the strain field. Generally speaking, the sizes measures from the dark region of BF TEM images indicate the fields of strain distribution giving larger figures than the real sizes of QDs.

The DF images show complementary contrast to BF images, as shown in Figures 3.19, 3.20 and 3.21. The (200) and (400) diffraction conditions have been discussed in chapter 2.2.3. The (200) and (400) diffraction conditions are sensitive to the chemical and strain contrast, respectively. However, the intensity of (200) beam is too weak to be visible, and the intensity of (400) is stronger than (200). For this reason, the (400) is chosen for the diffraction condition to form the DF images in this study.

Figures 3.22 and 3.23 depict the distribution of cross-sectional TEM strain field width and height of QDs. Sample 2 (5.72%) has the largest width and height of QDs of BF TEM image which coincides with the longest wavelength of PL spectra. Table 3.2 shows that the strain field width and height of QDs of samples 1, 2 and 3. It indicates that the dots sizes of Sb-doped in the buffer layer are larger than that without Sb-doped.

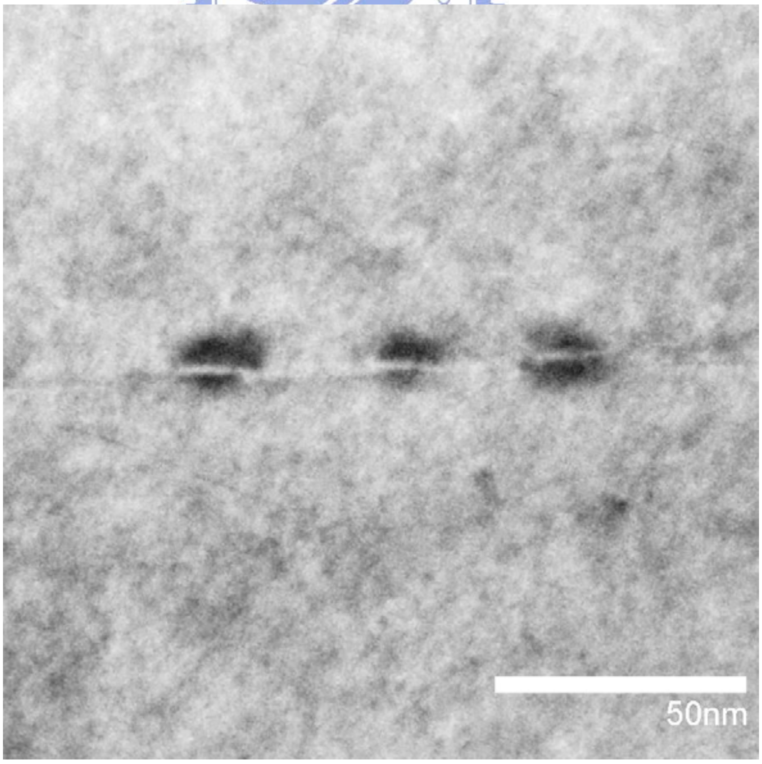

Figure 3.16 [100] Cross-sectional BF TEM image of sample 1 (0% Sb).

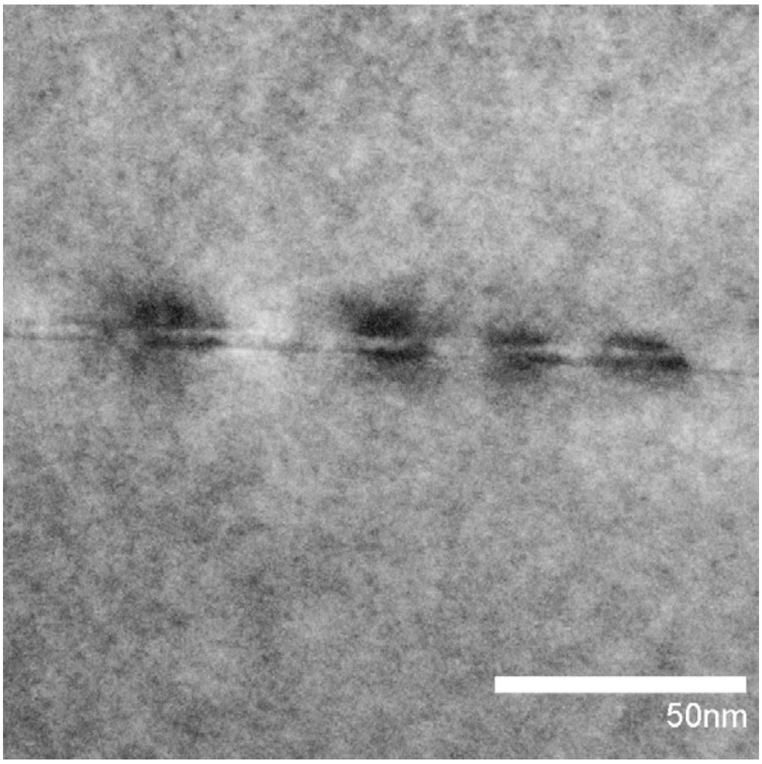

Figure 3.17 [100] Cross-sectional BF TEM image of sample 2 (5.72% Sb).

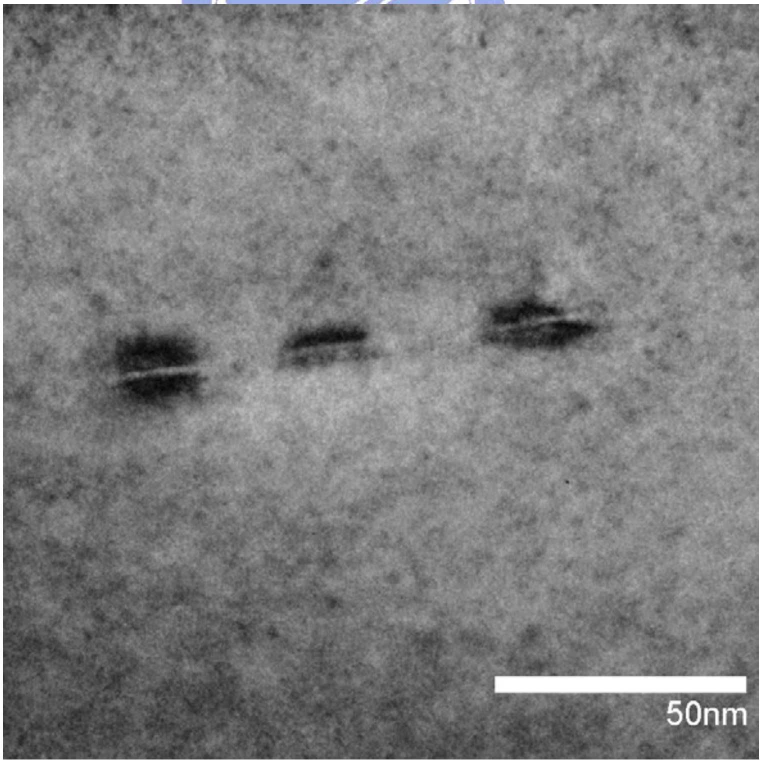

Figure 3.18 [100] Cross-sectional BF TEM image of sample 3 (11.44% Sb).

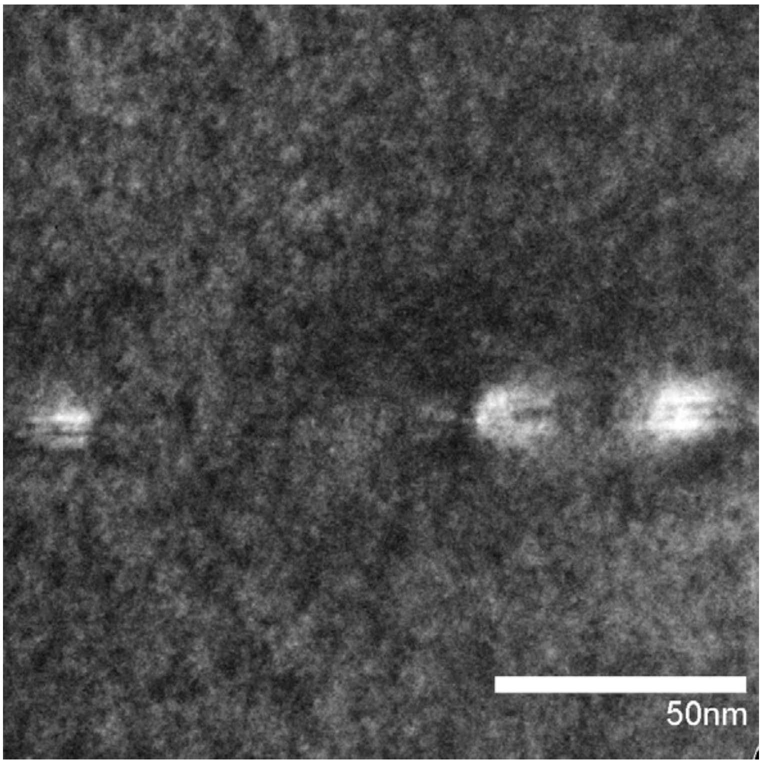

Figure 3.19 [100] Cross-sectional DF (400) TEM image of sample 1 (0% Sb).

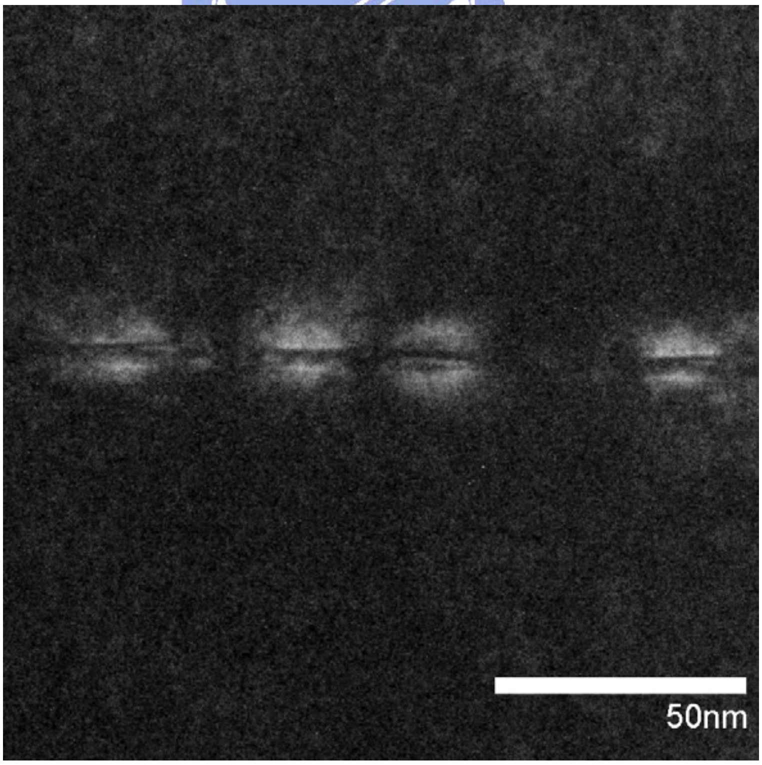

Figure 3.20 [100] Cross-sectional DF (400) TEM image of sample 2 (5.72% Sb).

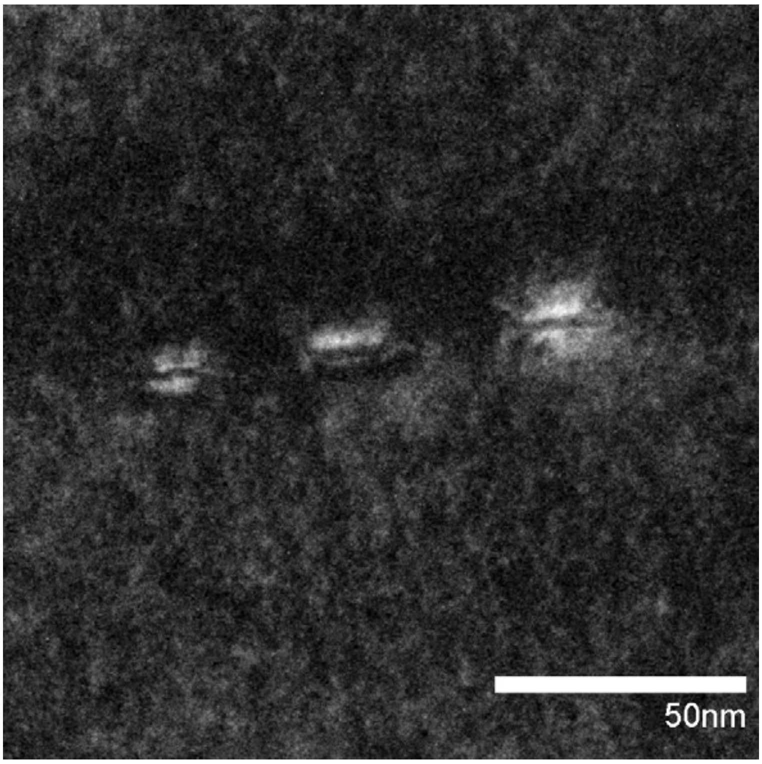

Figure 3.21 [100] Cross-sectional DF (400) TEM image of sample 3 (11.44% Sb).

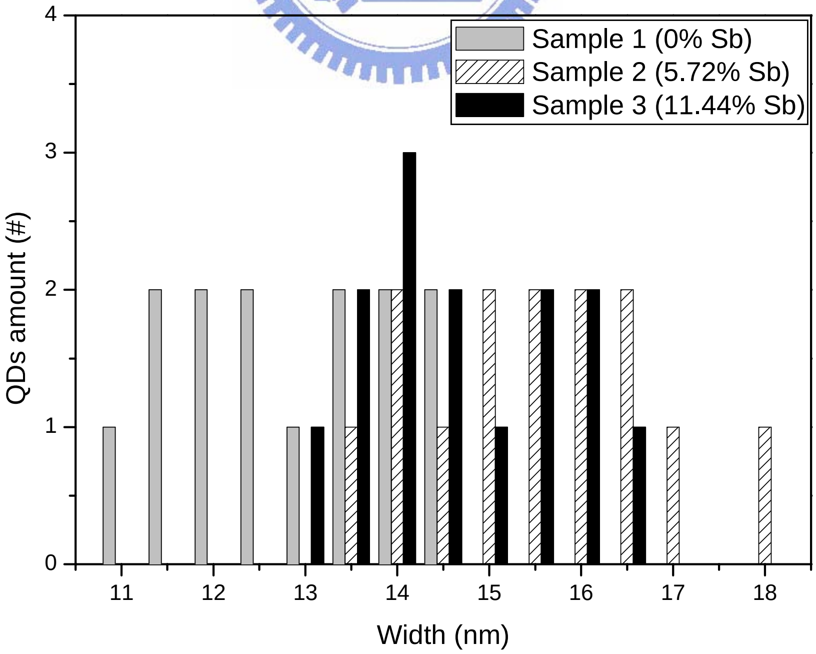

Figure 3.22 The distribution of cross-sectional TEM strain field width of QDs.

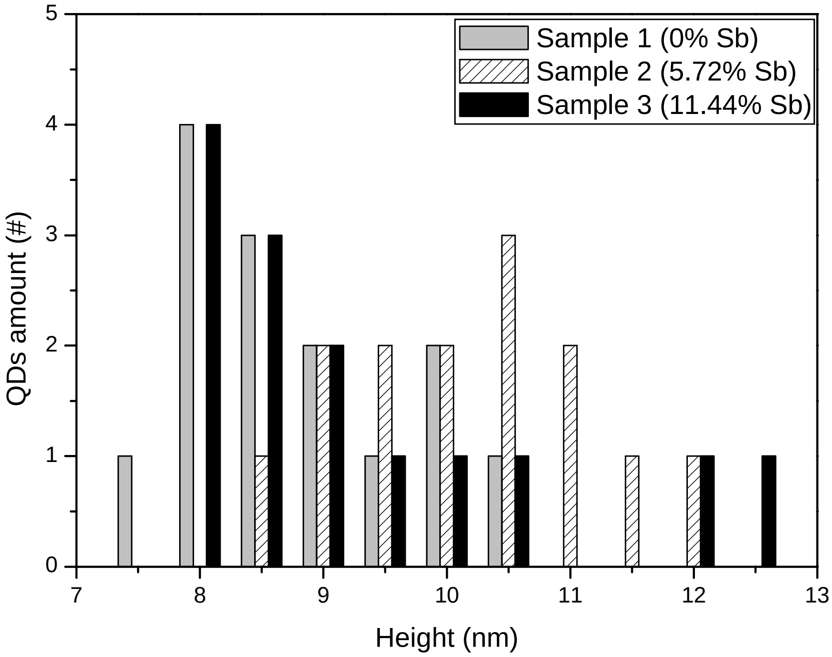

Figure 3.23 The distribution of cross-sectional TEM strain field height of QDs.

Table 3.2 Cross-sectional TEM of the strain filed width and height of QDs.

	Strain field width of cross-sectional TEM (nm)	Strain field height of cross-sectional TEM (nm)
Sample 1 (0% Sb)	11.9 ± 0.5	8.8 ± 0.3
Sample 2 (5.72% Sb)	15.5 ± 0.5	10.2 ± 0.3
Sample 3 (11.44% Sb)	14.7 ± 0.5	9.3 ± 0.3

3.4. Plan-view TEM

By tilting the specimen to two-beam conditions, in which only one diffracted beam is strong and the direct beam is the other strong spot in the pattern. Figures 3.24, 3.25 and 3.26 are the plan-view BF TEM images taken from samples 1, 2 and 3 under two-beam conditions. The two-beam conditions are not only necessary for contrast, and they also greatly simplify the interpretation of the images. These plan-view BF TEM images show that the field of strain distribution takes the bean shape for each sample. A bean with two half-moon-liked shapes represents a dot. But the shape of sample 2 (5.74% Sb) seems a little sharper than the other two samples. The dots density increases with the concentration of Sb in the buffer layer, but the dots density of three samples with the same order of magnitude and a nominal difference. The field of [100] and [010] strain distributions are shown in Figures 3.27 and 3.28. Table 3.3 depicts the strain field distribution and dots density of samples 1, 2 and 3.

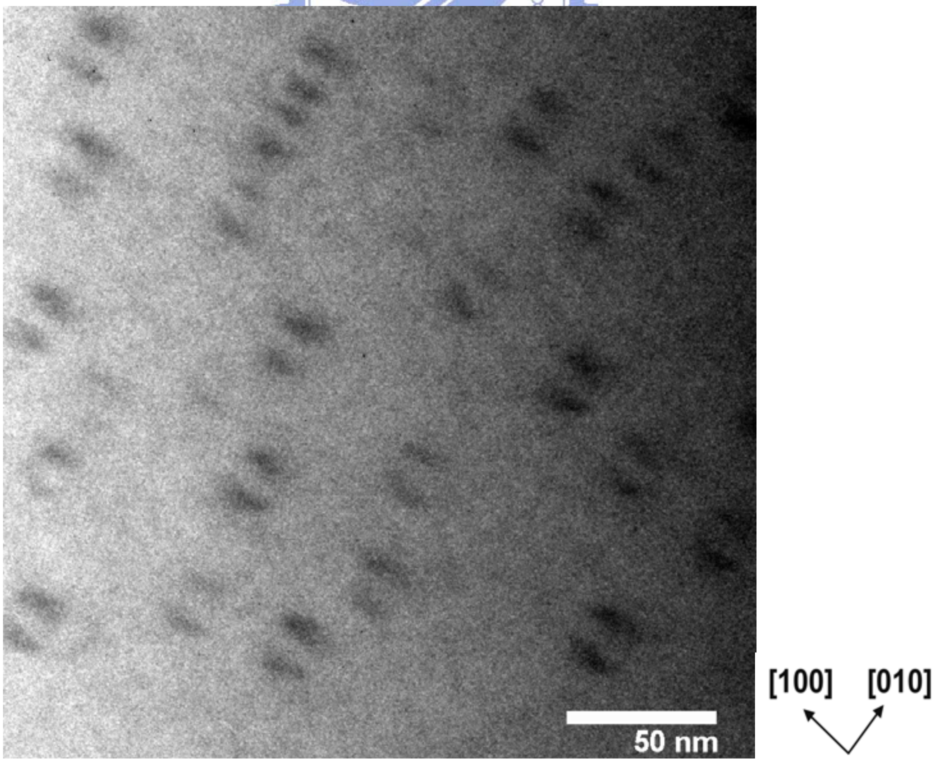

Figure 3.24 Plan-view BF TEM image of sample 1 (0% Sb) under two-beam conditions.

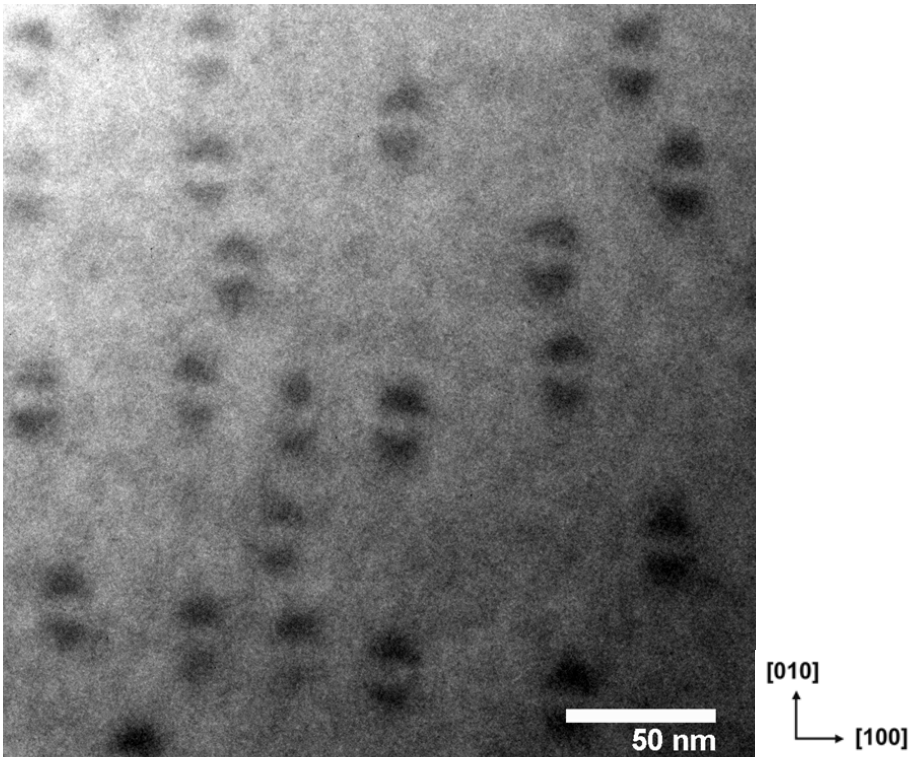

Figure 3.25 Plan-view BF TEM image of sample 2 (5.72% Sb) under two-beam conditions.

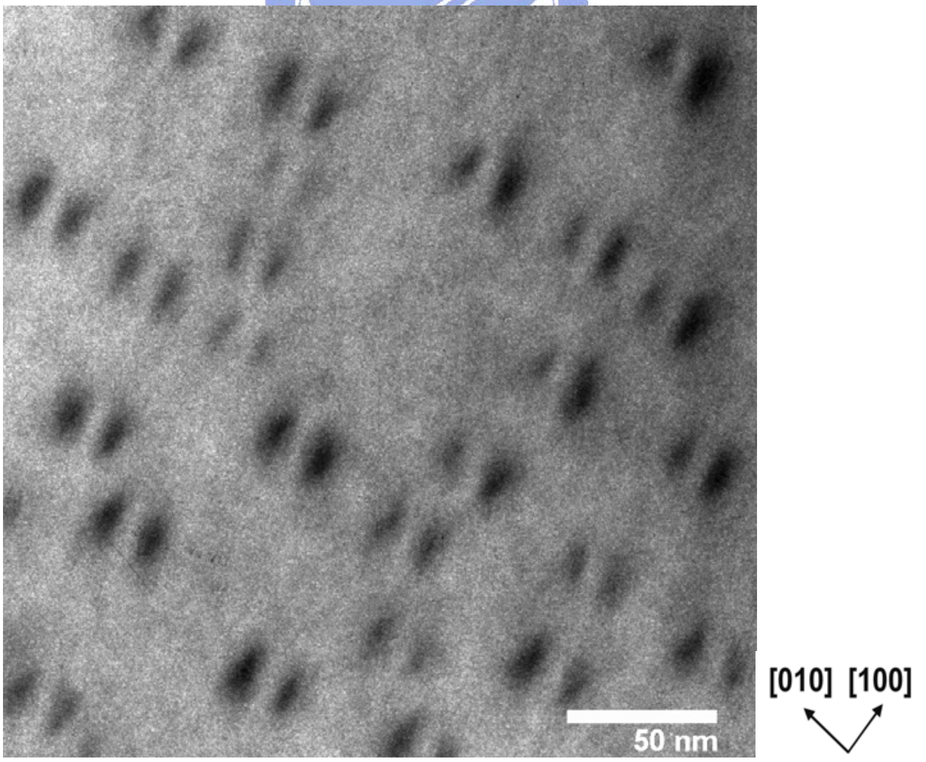

Figure 3.26 Plan-view BF TEM image of sample 3 (11.44% Sb) under two-beam conditions.

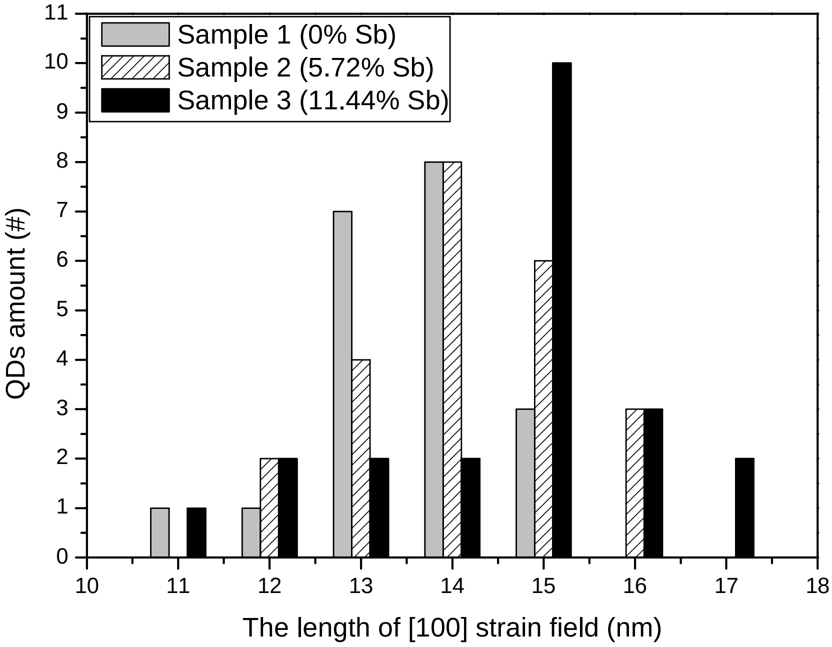

Figure 3.27 The distribution of plan-view TEM [100] strain field.

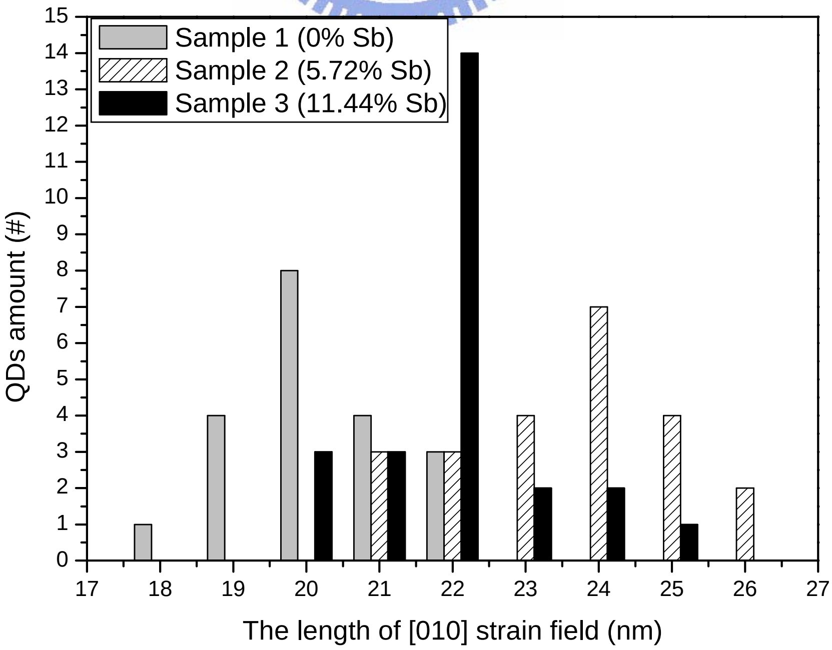

Figure 3.28 The distribution of plan-view TEM [010] strain field.

Table 3.3 Plan-view TEM of [100] and [010] strain filed and average density of QDs.

	[100] strain field (nm)	[010] strain field (nm)	Average density of plan-view (cm^{-2})
Sample 1 (0% Sb)	13.6 ± 0.5	20.2 ± 0.5	$3.4 \pm 0.2 \times 10^{10}$
Sample 2 (5.72% Sb)	14.2 ± 0.5	23.5 ± 0.5	$3.7 \pm 0.2 \times 10^{10}$
Sample 3 (11.44% Sb)	14.5 ± 0.5	22.0 ± 0.5	$4.0 \pm 0.2 \times 10^{10}$

3.5. The Analysis of Chemical Distribution

To characterize the chemical distribution of buried QDs, the HAADF-STEM and EDS are useful in analytical technique. Figure 3.29 is the cross-sectional HAADF-STEM image taken from sample 3 (11.44% Sb). An estimate of the composition can be made by combining STEM using a 1 nm probe with EDS, however EDS cannot provide an absolute composition value and, since STEM creates a two-dimensional image of the dot, assumptions are needed regarding the dot shape. Figure 3.30 displays the chemical distribution around the QD and the wetting layer of sample 3. Figure 3.31 shows that the atomic percentages and the EDS spectra of different regions of sample 3.

The region of the QD center in the sample 3 has the highest atomic percentage of In than other places and with a significant certainty of Sb. The In signal is also detected in the bottom of the dot but with a significant uncertainty of Sb. At the wetting layer, In is rich in the center. Moreover, the effect of beam broadening needed to be considered. With the Monte Carlo simulation, the diameters of beam broadening are about 12 and 16 nm for GaAs and InAs of 100 nm thickness of specimen. Hence, the concentration of In may contribute to the wetting layer and Sb may diffuse into InAs QDs.

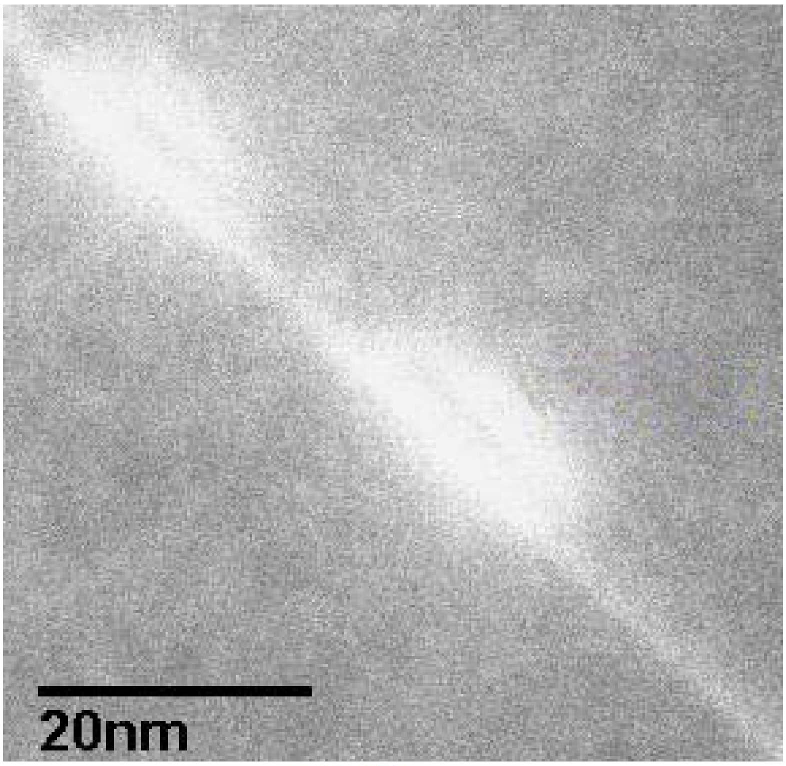

Figure 3.29 [100] Cross-sectional HAADF-STEM image of sample 3 (11.44% Sb).

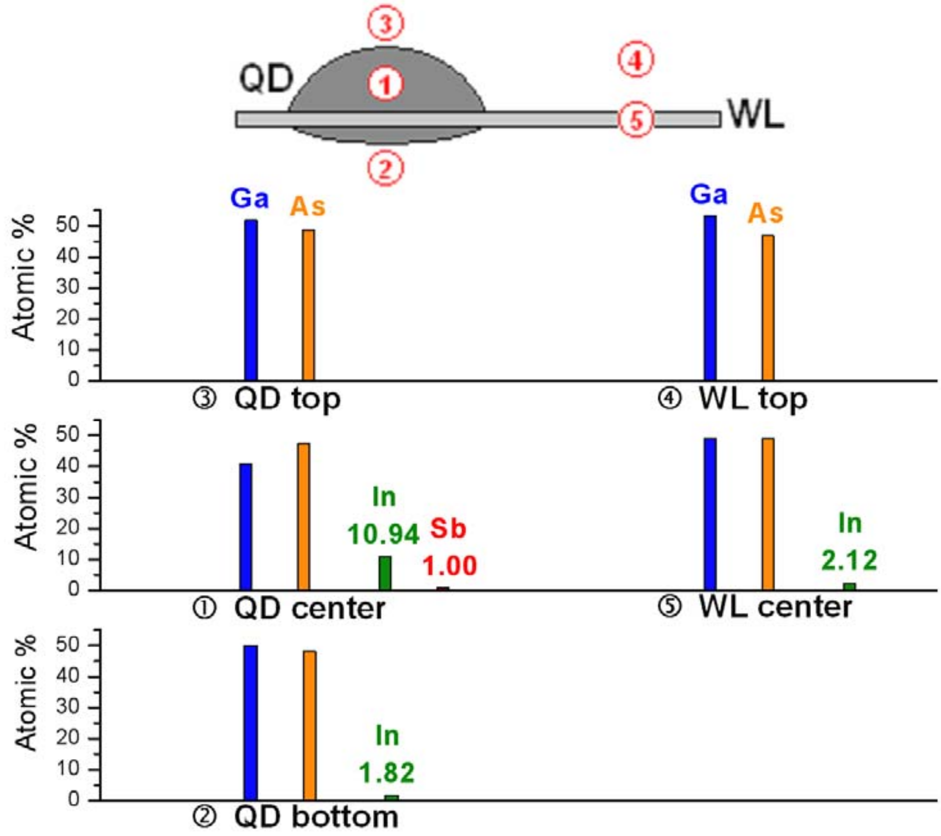

Figure 3.30 The chemical distribution around the QD and the wetting layer of sample 3.

① QD center

Element	Weight %	Atomic %
Ga	36.59	40.74
As	45.66	47.32
In	**16.18**	**10.94**
Sb	**1.57**	**1.00**

② QD bottom

Element	Weight %	Atomic %
Ga	47.81	50.11
As	49.23	48.01
In	**2.86**	**1.82**
Sb	**0.10***	**0.06***

③ QD top

Element	Weight %	Atomic %
Ga	50.35	51.95
As	50.65	48.63
In	**0.07***	**0.04***
Sb	**-**	**-**

④ WL top

Element	Weight %	Atomic %
Ga	51.40	53.19
As	48.62	46.82
In	**0**	**0**
Sb	**-**	**-**

⑤ WL center

Element	Weight %	Atomic %
Ga	46.63	48.98
As	50.02	48.89
In	**3.33**	**2.12**
Sb	**0.02***	**0.01***

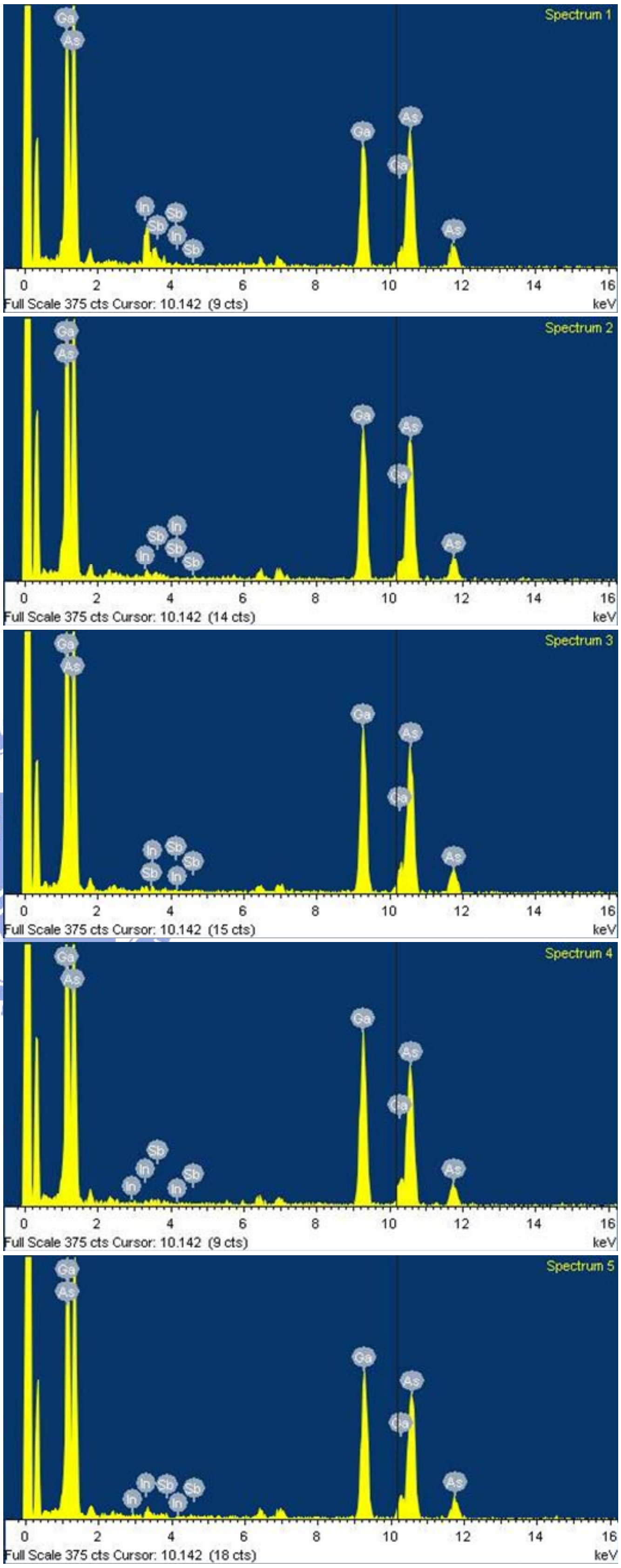

Figure 3.31 The atomic percentages and EDS spectra of different regions of sample 3.

(The star signal means the value is under the limit of resolution.)

In order to make sure that the EDS data are authentic, the Desktop Spectrum Analyzer (DTSA) is used to simulate the EDS spectrum with the chemical composition of the QD center. Figure 3.32 shows that the EDS spectra of the experimental result of the chemical composition in the dot center and the DTSA simulation of $In_{0.50}As_{0.35}Sb_{0.15}$. The specimen assumed that a 100-nm-thick. Due to the overlap of In and Sb x-ray peaks, the signals of In and Sb are hard to distinguish. However, in the experimental and the simulated results, the signals of In and Sb figure in the same position. Therefore, the real chemical composition in the QD center of EDS spectrum is believable. Moreover, the amount of Sb in the DTSA simulation is more than the original composition. It may conjecture that most of Sb atoms diffuse into InAs QDs, so that there are almost no signals of Sb in the QD bottom and WL center. From the above results, the HAADF-STEM and EDS data can demonstrate that the Sb atoms diffuse into InAs QDs.

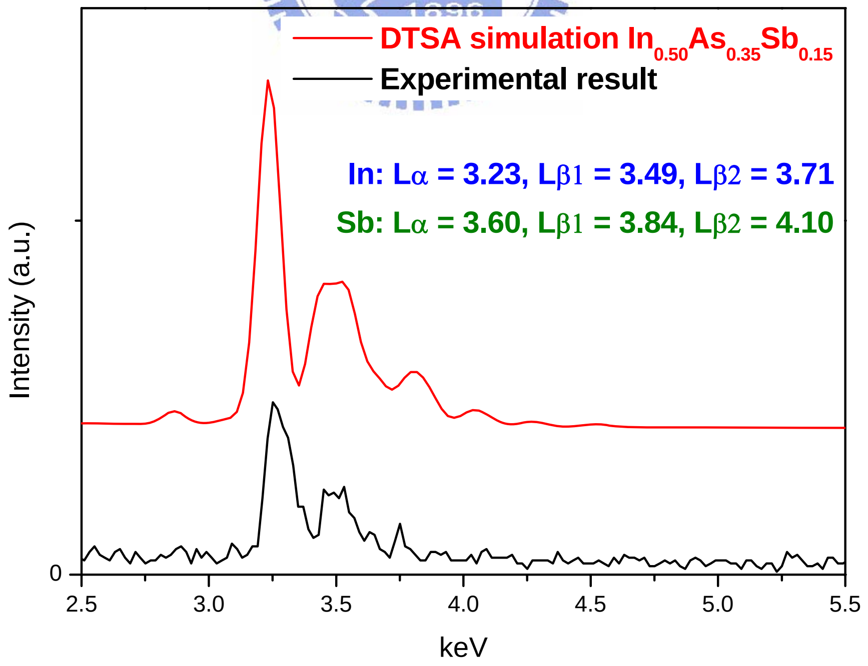

Figure 3.32 The EDS spectra of the experimental result of chemical composition in the dot center and the DTSA simulation of $In_{0.50}As_{0.35}Sb_{0.15}$.

3.6. Discussion

In general, the effect of Sb can enhance the growth of two-dimensional wetting layer and suppress the growth of the three-dimensional islands, resulting in the increase of the critical thickness from the transition of two-dimensional to three-dimensional growth mode. Therefore, it can increase the surface energy and reduce strain/stress between the epitaxy layers. It benefits the formation of defect free and highly uniform QD and lengthening the emission wavelength.

Based on the above theory, the goal of this study is trying to obtain the longer emission wavelength from QDs using a buffer layer of higher concentration of Sb. In the first place, it was expected that sample 3 (11.44% Sb) would have the longest wavelength and largest dots size than samples 1 (0% Sb) and 2 (5.74% Sb). However, the PL and TEM results show that sample 2 exhibits the longest wavelength and largest dots size, as listed in Table 3.1. Accordingly, there are two factors which have to be taken into consideration. The one is the influence of Sb diffusion into InAs QDs, and the other is the variation of lattice mismatch and surface energy while capping of the GaAs layer.

The SIMS data have no unambiguous evidence for the Sb atoms diffuse into InAs QDs. It can only support the viewpoint of Sb is resident roughly in the range of the QDs layer, wetting layer and buffer layer due to the depth resolution of SIMS. However, in some literature, it has been reported that Sb is rarely incorporate into quantum well and QDs [38]. In contrast, previous studies have shown that using Sb as a surfactant on GaAs, the density of InAs QDs can increase one order of magnitude [39, 40]. Nevertheless, the dots densities of samples 2 and 3 have no significant increases. The EDS data show that the Sb atoms exist in the QD center, and the simulation of DTSA has the same results. Thus, it is reasonable to assume that the Sb atoms diffuse into InAs QDs instead of being as a surfactant.

For PL and TEM measurements, there are some phenomena worthy to discuss. Figures 3.9 and 3.10 show that the PL emission wavelengths and FWHMs of the ES for sample 3

(11.44%) with 1.3 and 65 mW excitation powers at room temperature have almost the same values. The argument for the interpretation of the data is as following. If the Sb atoms diffuse into the QDs, the composition of dots alters to InAsSb. Hence, the lattice constant of InAsSb becomes larger than the original InAs dot. The excess compressive strain of a GaAs layer caps on the QDs layer that occurs the QDs of sample 3 will have a larger tensile strain of the direction parallel to the surface than samples 1 (0% Sb) and 2 (5.72% Sb). The dots of sample 3 are compressed into shorter height than that of sample 2. Therefore, the PL spectra show that the sample 2 has longer wavelengths than sample 3. The PL results seem consistent with the dots appearance of TEM images.

In cross-sectional and plan-view TEM images, the dots sizes and densities can be estimated from strain contrast. It is shown that the width and height of dots in sample 2 have larger sizes than those in samples 1 and 3, as listed in Table 3.2. The fields of strain distribution in plan-view images illustrate that sample 1 has the smallest dots, and the dot area in sample 2 is slightly larger than sample 3, as listed in Table 3.3. The dots density of the three samples exhibits the same order of magnitude of 10^{10} cm^{-2}, consistent with the PL data which show no increase of luminescence intensity with the Sb doping into the buffer layer.

Since the EDS data can be interpreted from the Sb diffusion in the InAs QDs, the experimental results of this work can be drawn from a derivable explanation as following, and a schematic diagram for the different stages of QDs formation is drawn in Figure 3.33. Figure 3.33 (a) shows that the morphology of QDs after formation. Then, the Sb atoms diffuse around the dots and into the dots, as shown in Figure 3.33 (b). Finally, Figure 3.33 (c) shows that while the capping of GaAs, the lattice mismatch of InAsSb dots with the capped GaAs results in the height decrease, such that the dot size becomes smaller for the case of sample 3.

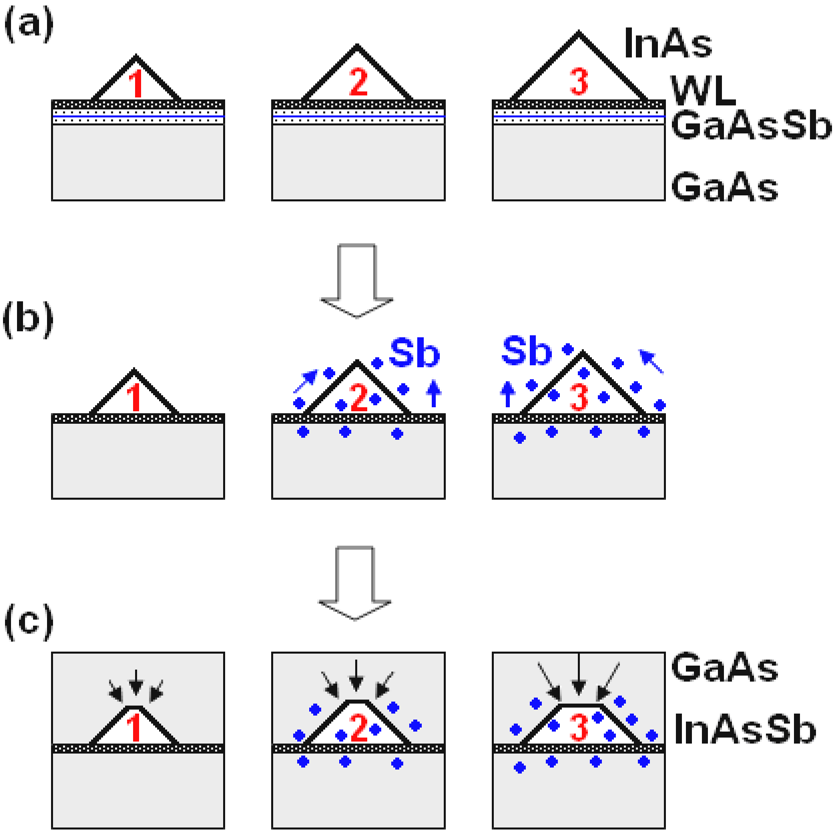

Figure 3.33 Schematic diagrams of (a) the formation of InAs QDs of samples 1 (0% Sb), 2 (5.72% Sb) and 3 (11.44% Sb), (b) the diffusion of Sb, (c) capping of GaAs layer.

Chapter 4 Summary

This work studies the effect of GaAsSb buffer layer of different Sb concentrations on the optical and structural properties of InAs QDs embedded in GaAs. The InAs/GaAs QD structures were grown by MBE, which contained the buffers of $GaAs_{1-X}Sb_X$ (X = 0%, 5.72%, and 11.44%) of 1 nm thickness on the GaAs substrates, and finally capped with a 300-nm-thick GaAs layer. In this thesis, SIMS and EDS were used to investigate the distribution of Sb in the QD structures. PL measurements and TEM images were performed to reveal the optical and structural properties of QDs.

The SIMS data support the viewpoint of Sb distribution roughly in the range of the QDs layer, wetting layer and buffer layer. The EDS data manifest the Sb atoms diffuse into InAs QDs with a significant In/Sb ratio up to 1/0.26. Therefore, most of the Sb atoms diffuse into the dots. PL measurements reveal that GaAsSb buffer layer in InAs QD structures results a wavelength redshift. The room temperature PL spectra show that the wavelength of samples 2 and 3 with GaAsSb buffer layer of 5.72% and 11.44% Sb is 1.22 and 1.21 μm from InAs QDs embedded in GaAs. TEM images show that the dots size increases with the concentration of Sb in the buffer layer, but with an insignificant increase in density. From cross-sectional TEM images, the dots width and height are 15.5 and 10.2 nm in sample 2, and 14.7 and 9.3 nm in sample 3. But the dots width and height in sample 1 without GaAsSb buffer layer in the QD structures are found to be 11.9 and 8.8 nm. These results demonstrate that the dots sizes in Sb-doped samples are larger than those in the pure InAs QDs. From plan-view TEM images, the dot densities in three samples are found to be $3.4\sim4.0\times10^{10}$ cm^{-2}.

In conclusion, PL and TEM measurements were performed to reveal that the longer wavelength and the larger dots size of InAs QDs with GaAsSb buffer layer in QD structures. The HAADF-STEM with EDS analysis proves that the Sb diffusion in InAs QDs. With the above of solid results, the tunable GaAsSb buffer layer results in an enhancement on the size of QDs.

The future work can be focused on the follows: The PL excitation and the absorption spectra can realize what factors affect the excited state. The HRTEM and the Raman measurements may get the strain in the buffer layer, the wetting layer and the QDs. With the HAADF-STEM, the three dimensional tomography, the HRTEM and the EELS mapping can characterize the shape and size of QDs, and the thickness of the buffer and wetting layers.

References

[1] L. Esaki and R. Tsu, "Superlattice and Negative Differential Conductivity in Semiconductors", IBM Journal Reseaech Development, 14, 61 (1970).

[2] Weng W. Chow, and Marek Osinski, Physics and Simulation of Optoelectronic Devices II, SPIE, 1994.

[3] Vitaly A. Shchukin, Nikolai N. Ledentsov, Dieter Bimberg, Epitaxy of Nanostructures, Springer, Berlin, 2004.

[4] István Daruka and Albert-László Barabási, "Equilibrium phase diagrams for dislocation free self-assemble quantum dots", Applied Physics Letters, 72, 2102 (1998).

[5] Kazuo Nakajima, "Equilibrium Phase Diagrams for Stranski-Krastanov Structure Mode of III-V Ternary Quantum Dots", Japanese Journal of Applied Physics, 38, 1875 (1999).

[6] B. R. Bennett, B. V. Shanabrook, P. M. Thibado, L. J. Whitman, and R. Mengo, "Stranski-Krastanov growth of InSb, GaSb, and AlSb on GaAs Structure of the wetting layers", Journal of Crystal Growth, 175/176, 888 (1997).

[7] A. Rosenauer, Transmission Electron Microscopy of Semiconductor Nanostructures: Analysis of Composition and Strain State Springer, Heidelberg, Berlin, 2003.

[8] Donald A. Neamen, Semiconductor Physics and Devices: Basic Principles, McGraw-Will, Boston, 2003.

[9] Y. Nakata, K. Mukai, M. Sugawara, K. Ohtsubo, H. Ishikawa, and N. Yokoyama, "Molecular beam epitaxial growth of InAs self-assembled quantum dots with light-emission at 1.3 μm", Journal of Crystal Growth, 208, 93 (2000).

[10] L. Chu, M. Arzberger, G. Böhm, and G. Abstreiter, "Influence of growth conditions on the photoluminescence of self-assembled InAs/GaAs quantum dots", Journal of Applied Physics, 85, 2355 (1999).

[11] Vladimir I. Trofimova, Hee Seok Parkb, and Jong-Il Kimc, "Growth and optical properties of InAs/GaAs quantum dot structures", Applied Surface Science, 226, 45 (2004).

[12] A. A. Quivy, M. J. da Silva, T. E. Lamas, E. C. F. da Silva, and J. R. Leite, "Large self-assembled InAs/GaAs quantum dots with an optical emission above 1.3 μm", Physica status solidi (c), 1, S133 (2004).

[13] R. Ohtsubo and K. Yamaguchi, "High quality InAs quantum dots covered by InGaAs/GaAs hetero-capping layer", Physica status solidi (c), 0, 939 (2003).

[14] P. B. Joyce, T. J. Krzyzewski, G. R. Bell, and T. S. Jones, "Optimizing the growth of 1.3 μm InAs/GaAs quantum dots", Physical Review B, 64, 235317 (2001).

[15] Kouichi Akahane, Naokatsu Yamamoto, and Naoki Ohtani, "Long-wavelength light emission from InAs quantum dots covered by GaAsSb grown on GaAs substrates", Physica E, 21, 295 (2004).

[16] H. Y. Liu, M. J. Steer, T. J. Badcock, D. J. Mowbray, M. S. Skolnick, P. Navaretti, K. M. Groom, M. Hopkinson, and R. A. Hogg, "Long-wavelength light emission and lasing from InAs/GaAs quantum dots covered by a GaAsSb strain-reducing layer", Applied Physics Letters, 86, 143108 (2005).

[17] J. M. Ripalda, D. Granados, Y. González, A. M. Sánchez, S. I. Molina, and J. M. García, "Room temperature emission at 1.6 μm from InGaAs quantum dots capped with GaAsSb", Applied Physics Letters, 87, 202108 (2005).

[18] Hitoshi Shimizu and Shanmugam Saravanan, "Buffer-material dependence of InAs quantum dots on GaAs substrate", Applied Physics Letters, 88, 041119 (2006).

[19] Y. Sun, S. F. Cheng, G. Chen, R. F. Hicks, J. G. Cederberg, and R. M. Biefeld, "The effect of antimony in the growth of indium arsenide quantum dots in gallium arsenide (001)", Journal of Applied Physics, 94, 053503 (2005).

[20] Denis Guimard, Masao Nishioka, Shiro Tsukamoto, and Yasuhiko Arakawa, "Effect of antimony on the density of InAs/Sb:GaAs(100) quantum dots grown by metalorganic chemical-vapor deposition", Journal of Crystal Growth, 298, 548 (2007).

[21] Koichi Yamaguchi and Toru Kanto, "Self-assembled InAs quantum dots on GaSb/GaAs(001) layers by molecular beam epitaxy", Journal of Crystal Growth, 275, 2269 (2005).

[22] István Daruka and Albert-László Barabási, "Dislocation-Free Island Formation in Heteroepitaxial Growth: A Study at Equilibrium", Physical Review Letters, 79, 3708 (1997).

[23] A. Benninghoven, F. G. Rudenauer, and H. W. Werner, Secondary ion mass spectrometry : basic concepts, instrumental aspects, applications and trends, John Wiley & Sons, New York, 1987.

[24] John C. Vickerman, Surface Analysis - The Principal Techniques, John Wiley & Sons, Chichester, 1997.

[25] KLAUS D. MIELENZ, Measurement of photoluminescence, Academic Press, London ; New York, 1982.

[26] Karsten Hannewald, Stephan Glutsch, Friedhelm Bechstedt, "Nonequilibrium theory of photoluminescence excitation spectroscopy in semiconductors", physica status solidi (b), 238, 517 (2003).

[27] Sidney Perkowitz, Optical characterization of semiconductors/Infrared, raman, and photoluminescence spectroscopy, Academic Press, London, 1993.

[28] David B. Williams and C. Barry Carter, Transmission electron microscopy, Plenum Press, New York, 1996.

[29] P. F. Fewster, V. Holý, and D. Zhi, "Composition determination in quantum dots with in-plane scattering compared with STEM and EDX analysis", Journal of Physics D, 36, A217 (2003).

[30] K. Scheerschmidt and P. Werner, Nano-Optoelectronics: Concepts, Physics and Devices, NanoScience and Technology, 67-98. Springer, Heidelberg, Germany, 2002.

[31] J. Cagnon, P. A. Buffat, P. A. Stadelmann, K. Leifer, "Theoretical and experimental limits of quantitative analysis of strain and chemistry of inGasAs/GaAs layers using (200) dark-field TEM imaging", Inst. Phys. Conf. Ser., 180, 203 (2003).

[32] R. Beanland, "Dark field transmission electron microscope images of Ⅲ-Ⅴ quantum dot structures", Ultramicroscopy, 102, 115 (2005).

[33] Y. Wang, H. S. Djie, and B. S. Ooi, "Interdiffusion in InGaAsSb/AlGaAsSb quantum wells", Journal of Applied Physics, 98, 073508 (2005).

[34] N. A. Bert, V. V. Chaldyshev, Yu. G. Musikhin, V. V. Preobrazhenskii, M. A. Putyato, B. R. Semyagin, and P. Werner, "In–Ga intermixing in low-temperature grown GaAs delta doped with In", Applied Physics Letters, 74, 1442 (1999).

[35] V. V. Chaldyshev, N. A. Bert, Yu. G. Musikhin, A. A. Suvorova, V. V. Preobrazhenskii, M. A. Putyato, B. R. Semyagin, P. Werner, and U. Gösele, "Enhanced As-Sb intermixing of GaSb monolayer superlattices in lowtemperature grown GaAs", Applied Physics Letters, 79, 1294 (2001).

[36] Chun-Yuan Huang, Tzu-Min Ou, Shu-Ting Chou, Cheng-Shuan Tsai, Meng-Chyi Wu, Shih-Yen Lin, and Jim-Yong Chi, "Temperature dependence of carrier dynamics for InAs/GaAs quantum dot infrared photodetectors", Journal of Vacuum Science and Technology B, 23, 1909 (2005).

[37] Chang-Myung LEE Suk-Ho CHOI, Sam-Kyu NOH, Joo In LEE, Jin-Soo KIM, and Il-Ki HAN, "Three-Modal Size Distribution of Self-assembled InAs Quantum Dots", Japanese Journal of Applied Physics, 44, (2005).

[38] P. Aivaliotis, L. R. Wilson, E. A. Zibik, J. W. Cockburn, M. J. Steer, and H. Y. Liu, "Enhancing the dot density in quantum dot infrared photodetectors via the incorporation of antimony", Applied Physics Letters, 91, 013503 (2007).

[39] Denis Guimard, Masao Nishioka, Shiro Tsukamoto, and Yasuhiko Arakawa, "High density InAs/GaAs quantum dots with enhanced photoluminescence intensity using antimony surfactant-mediated metal organic chemical vapor deposition", Applied Physics Letters, 89, 183124 (2006).

[40] Toru Kanto and Koichi Yamaguchi, "In-plane self-arrangement of high-density InAs quantum on GaAsSb/GaAs(001) by molecular beam epitaxy", Journal of Applied Physics, 101, 094901 (2007).

Appendixes

A. Monte Carlo Simulation

Program : SS_MT_95 (Single Scattering Monte Carlo Simulation)

The conditions of Monte Carlo simulation — Foil

a. GaAs

1. Beam voltage : 200 kV
2. Atomic number : 32
3. Atomic weight : 72.3223
4. Target density : 5.316 g/cc
5. Foil thickness : 100 nm
6. Specimen tilt : 0 degree
7. Traj. number : 100

b. InAs

1. Beam voltage : 200 kV
2. Atomic number : 41
3. Atomic weight : 94.8708
4. Target density : 5.66 g/cc
5. Foil thickness : 100 nm
6. Specimen tilt : 0 degree
7. Traj. number : 100

The diameters of beam broadening are about 12 and 16 nm for GaAs and InAs with an average number for ten times simulations.

B. Desktop Spectrum Analyzer Simulation

The conditions of DTSA simulation — Thin target specimen

1. Beam voltage : 200.00 kV
2. NanoAmps Faraday : 1.00
3. Life time : 100.00 s
4. Density : 5.66 g/cc
5. Thickness : 100.00 nm
6. Other setting :

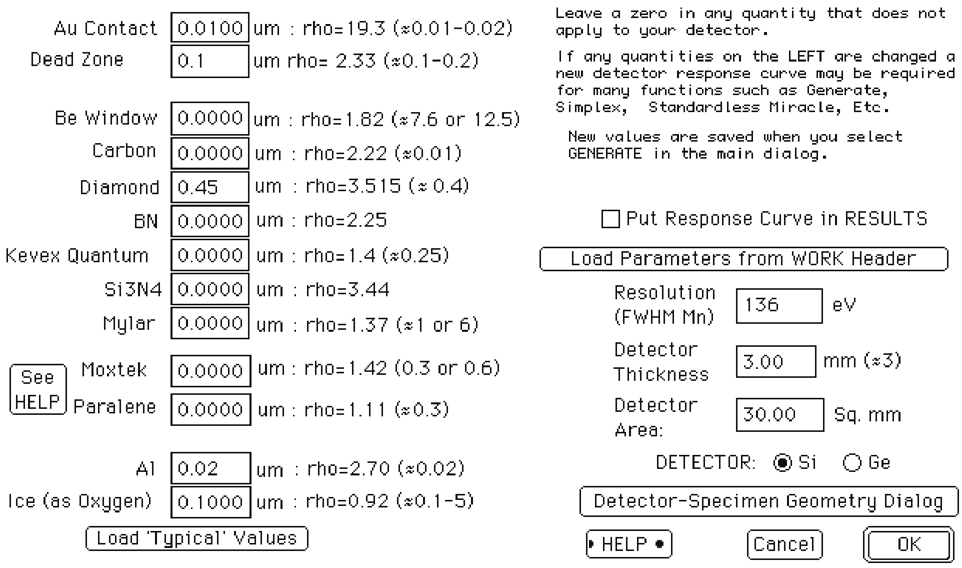

Au Contact 0.0100 um : rho=19.3 (≈0.01-0.02)
Dead Zone 0.1 um rho= 2.33 (≈0.1-0.2)
Be Window 0.0000 um : rho=1.82 (≈7.6 or 12.5)
Carbon 0.0000 um : rho=2.22 (≈0.01)
Diamond 0.45 um : rho=3.515 (≈ 0.4)
BN 0.0000 um : rho=2.25
Kevex Quantum 0.0000 um : rho=1.4 (≈0.25)
Si3N4 0.0000 um : rho=3.44
Mylar 0.0000 um : rho=1.37 (≈1 or 6)
Moxtek 0.0000 um : rho=1.42 (0.3 or 0.6)
Paralene 0.0000 um : rho=1.11 (≈0.3)
Al 0.02 um : rho=2.70 (≈0.02)
Ice (as Oxygen) 0.1000 um : rho=0.92 (≈0.1-5)

Leave a zero in any quantity that does not apply to your detector.

If any quantities on the LEFT are changed a new detector response curve may be required for many functions such as Generate, Simplex, Standardless Miracle, Etc.

New values are saved when you select GENERATE in the main dialog.

☐ Put Response Curve in RESULTS

Resolution (FWHM Mn) 136 eV
Detector Thickness 3.00 mm (≈3)
Detector Area: 30.00 Sq. mm
DETECTOR: ● Si ○ Ge

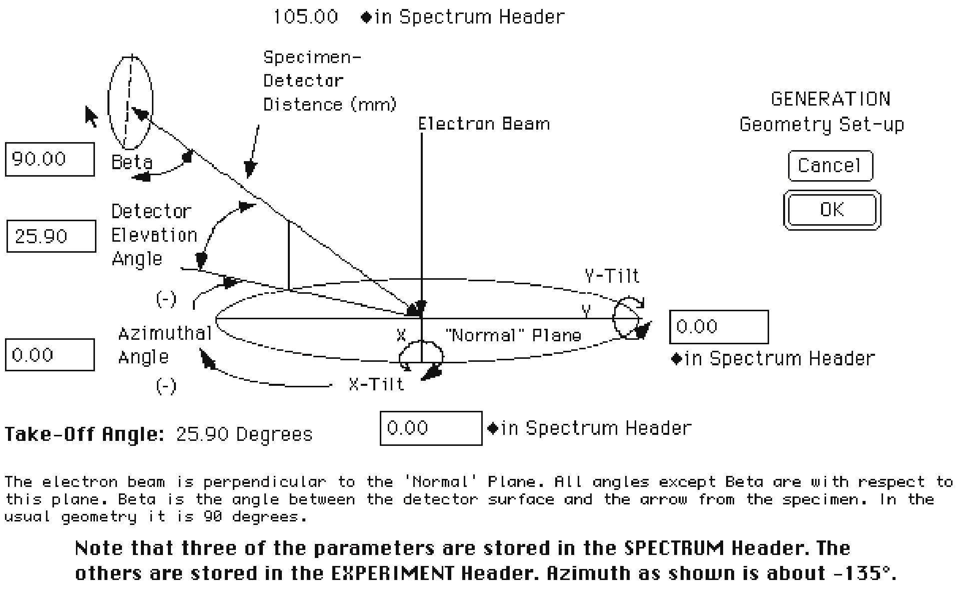

Specimen-Detector Distence (mm) 105.00 ◆in Spectrum Header
Beta 90.00
Detector Elevation Angle 25.90
Azimuthal Angle 0.00
Y-Tilt 0.00 ◆in Spectrum Header
X-Tilt 0.00 ◆in Spectrum Header

Take-Off Angle: 25.90 Degrees

The electron beam is perpendicular to the 'Normal' Plane. All angles except Beta are with respect to this plane. Beta is the angle between the detector surface and the arrow from the specimen. In the usual geometry it is 90 degrees.

Note that three of the parameters are stored in the SPECTRUM Header. The others are stored in the EXPERIMENT Header. Azimuth as shown is about -135°.